Universitat Politècnica de Catalunya

Departament de Física i Enginyeria Nuclear

Departament de Física Aplicada

Programa de doctorat:

Ciència i Tecnologia Aeroespacial

Improvement of corrosion and mechanical properties of amorphous steels by microalloying and nanocrystallization

Milad Madinehei

Supervised by

Dr. Pere Bruna and Dr. Eloi Pineda

To my Parents,

Acknowledgements

It is a great pleasure to thank the many people that supported me during my Ph.D. studies.

I would first like to express my deep gratitude to my supervisors, Dr. Pere Bruna and Dr. Eloi Pineda, for their encouragement, constructive guidance and words of motivation throughout the duration of this research study and moreover for the inspiration they provided to ensure the completion of this work. Their expertise, availability to discuss ideas and willingness to give of their knowledge were instrumental. For this, I will be eternally grateful.

I would also like to express my thanks to Professor Daniel Crespo who followed my activities carefully and with enormous patience. It was his hardworking attitude, and positive energy that motivated me to work harder. I appreciate all his contributions of time and ideas to make my journey towards the Ph.D. degree. Without his critical comments and patient instructions the completion of the present dissertation would not have been possible. I learned a lot from his exemplary leadership, high standards for research, professionalism, and thoughtful guidance.

I really appreciated the opportunity to collaborate with the Energy Materials and Interfaces group headed by Dr. Franck Renner at the Max Planck Institute for Iron research. Thanks to Dr. Renner for being such a wonderful host. It is truly an honor to work with such an outstanding man who is willing to share his wealth of knowledge and his extensive personal

experience. During my stay in Germany, I found very valuable colleagues with whom I shared work. In particular, it was a great pleasure to work with Dr. Jazmin Duarte, who supervised my experimental activity in the laboratories and who always gave me her precious aid.

Special thanks go to Dr. Jordi Sort of the Department of physics, Universitat Autònoma de Barcelona (UAB) for his help and guidance in nano-indentation testing.

My work was supported by Generalitat de Catalunya grant FI-DGR. I would also like to acknowledge the financial support from CICYT grant MAT2010-14907 and Generalitat de Catalunya grants 2009SGR1225 and 2009SGR1251. Therefore, I express my gratitude to all of these entities and agencies for their support to my work.

I would like to thank my lovely officemates: Araceli, Estel, Anna, Shervin, Gabriela, Chaoren, Fuqiang, Ruxandra, Isa and Francesc for their help and friendship. I had a wonderful time with you. You are the best!

Last but not least, my deepest gratitude goes to my family without whom I couldn't have achieved my goals. I would like to express my eternal love to my parents, Parvin and Mohammad, for their encouragement, patience and support. Special thanks are due to my one and only loving sister Mahsa who always strengthened my morale by standing by me in all situations.

Table of Content:

List of figures

List of Tables

1 Introduction

1.1 Metallic glasses

Solids are characterized by the length scale arrangement of their components in which they are generally locked to their positions. Crystalline structure is formed by repeating patterns of atoms, ions or molecules across its whole volume. Periodicity of the structural units of the substance over long atomic distances is referred to as long-range order. Amorphous solids are non-crystalline solids whose atomic packing do not exhibit long-range order [1].

Amorphous metallic alloys have attracted wide attention in modern materials science because of their intrinsic and technological properties. These amorphous metals and metal alloys evince unique magnetic, mechanical, electrical and chemical properties which differ from those of their crystalline counterparts [2]. To date, these novel materials have already been successfully utilized in diverse areas. The principal applications are: electronics equipment, magnetic devices, luxury goods, biomedical devices and sporting goods.

There are different possible techniques to prepare non-crystalline materials [3]. These techniques are based on rapid extracting the thermal energy from the gaseous or liquid state. These materials can be obtained by vapor-state or solid-state processing methods and quenching from the liquid state. A non-

crystalline solid obtained by continuous melt-quenching is called *glass*. In 1960 [4] Duwez and his coworkers prepared the first metallic glass by rapid solidification technique. They produced a binary metallic glass in the Au-Si system at very high cooling rates approaching 10^6 K/s^{-1}. The metallic melts have a high propensity to crystallize and therefore, high cooling rates are required to avoid crystallization and because the cooling rate is inversely proportional to the diameter of the ingot, this limits the size of the glasses to the order of few centimeters in at least one dimension [5]. At high cooling rates (of the order of 10^6 K/s^{-1}) most of the glass-forming alloys can only be produced in a limited number of shapes (typically ribbons, wires, or sheets). Although several attempts have been made to overcome the limitation of size in metallic glasses, producing metallic glasses in bulk shape with three-dimensional centimeter-scale was a moot point for many years. These attempts mostly focused on the liquid metal quenching methods and compositional modifications. In 1960s ternary quasi-bulk metallic glass in Pd-Cu-Si system was prepared but the critical diameter was only 1 mm [6]. A notable advance was made in 1984 by Turnbull group who were able to produce $Pd_{40}Ni_{40}P_{20}$ alloys with a diameter of 5 mm [7]. They decreased heterogeneous nucleation by fluxing molten $Pd_{40}Ni_{40}P_{20}$ with dehydrated B_2O_3 and were thus able to produce metallic glass with a critical cooling rate as low as about 10 K/s. Although many efforts were done until the late 1980s to fabricate metallic glasses in bulk shapes, the critical diameters of these materials did not exceed 10 mm. In the late 1980s and 1990s new quaternary and quinary metallic glasses with critical cooling rates of less than 100 K/s, were developed By Johnson and Inoue [8, 9]. These findings enabled the casting of massive samples and led to the first bulk metallic glasses (BMGs).

Although the size and shape limitation of metallic glasses have restricted their structural use, the combination of their properties makes them suitable for a variety of technological applications. Amorphous ribbons, sheets and wires are frequently used in several areas of engineering because they possess the characteristics of amorphous materials and are able to ensure high ratio between strength and weight in the applications requiring a high strength-to-weight ratio [10, 11]. There are principally two classifications of metallic glasses [12]: metal-metal and metal-metalloid systems. In the metal-metal type metallic glasses, two transition metals are involved. They consist of one early transition metal (50-90 at %) and one late transition metal. Typical alloys in this category are $Fe_{90}Zr_{10}$, $Ni_{60}Nb_{40}$, $Mg_{70}Zn_{30}$, $Cu_{57}Zr_{43}$ and $La_{80}Au_{20}$. The second class of metallic glasses are formed by combination of one or different types of metals (~80 at %) and metalloids (typically Si, B, C and P). Some examples for this category are $Au_{80}Si_{20}$, $Pd_{80}Si_{20}$, $Fe_{80}B_{20}$, $Pd_{77}Cu_6Si_{17}$, $Fe_{40}Ni_{40}B_{20}$, $Ni_{75}Si_8B_{17,}$ $Fe_{70}Cr_{10}P_{13}C_7$ etc.

The amorphous structure characteristic of metallic glasses is most clearly evidenced in a diffraction experiment such as X-ray diffraction (XRD) or with a transmission electron microscopy (TEM). Figure 1.1 shows an example of a High Resolution TEM (HRTEM) image of an amorphous material, as well as the corresponding Selected Area Diffraction (SAED) Pattern. One cannot observe any effects due to crystallization or long range ordering and in the SAED pattern only a broad halo typical of amorphous structures can be seen.

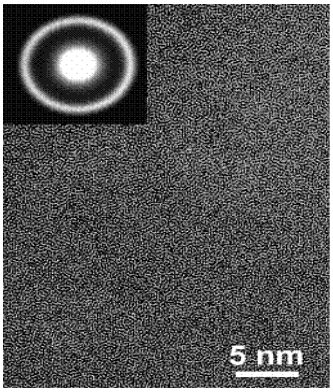

Figure 1.1 High-resolution TEM image of glassy phase. The inset shows a selected-area electron diffraction pattern.

1.2 Fe-based metallic glasses

Amongst different types of metallic glasses, Fe-based metallic glasses have attracted considerable attention due to their singular combination of properties such as superior strength, high hardness, resistance to corrosion and wear, soft magnetic properties and relatively low priced elements [12, 13]. Composites based on ferrous metallic glasses containing second phases reinforced in amorphous matrix, exhibit even better mechanical properties in some cases [14]. Also Nanocrystalline Fe-based materials produced by solid state reaction (crystallization) of amorphous phase are potential candidates for magnetic applications because of their soft (or hard) magnetic properties [15, 16]. These nanostructured materials exhibit excellent soft magnetic properties including relatively high saturation magnetization (M_s) and permeability (μ), as well as low coercive force (H_c) and core loss (W).

However, most of the Fe-based metallic glasses exhibit almost no plastic strain and strain hardening even in compression when tested at ambient temperature [17]. Also a vast majority of this family of amorphous materials show low glass forming tendency which restricts the potential of using them as engineering materials. The largest section thickness obtained in Fe-based metallic glasses is only about 16 mm [18], while the largest diameter achieved in Zr and Pd-based metallic glasses exceeds several centimeters [19].

Metal-metal type Fe-based amorphous alloys containing less than 15 at% of Zn or Hf in powder or ribbon shapes have been investigated since 70s [12]. These binary amorphous alloys exhibit some novel magnetic properties and high thermal stabilities. However the critical dimensions of these amorphous alloys have not been larger than 20 μm due to their poor glass forming ability even in their eutectic compositions.

Since $Fe_{80}B_{20}$ amorphous ribbons have been prepared by melt-spinning technique this composition is often used as the starting alloy for composition selection in Fe-metalloid systems. Bulk ferrous amorphous alloys are characterized by the presence of approximately 20-25 at% of metalloids (B, C, P or Si) and the substitution of Fe by other metallic elements depending on the desired properties. In order to enable superior performance under multi-functional conditions, there have been many attempts made to raise the ease of glass forming of this family of amorphous alloys to produce bulk Fe-based metallic glasses. Fe-based bulk metallic glasses contain glass forming metal elements such as Al, Mo, Nb, Ga and Y which are added to Fe with the amounts ranging 1-30%. The first report on Fe-based bulk metallic glasses

was reported in 1995 [20] where Fe-(Al,Ga)-(P,C,B,Ge,Si) rods with 1-2 mm diameters were prepared by copper mold casting. Since then a large number of Fe-based bulk metallic glasses have been synthesized with the critical diameter of over 10 mm which literally can be called *bulk.* Although conventional steels are the most important group of engineering alloys with excellent properties for industrial applications, some amorphous steels could overtake their crystalline counterparts in many good properties. The appellation of amorphous and conventional steels is because of the carbon element, but the presence of carbon in amorphous and conventional steels has two different reasons. Carbon is traditionally added to conventional steels as a hardening agent. In the case of amorphous steels, C is added to the alloy to enable glass formation. Comparing the maximum attainable thickness of amorphous steels and C-free Fe-based metallic glasses [13] it can be concluded that the size limitation of Fe-based amorphous alloys has been greatly overcome in C-added alloys. Without carbon, the Fe-based amorphous alloys can be cast only into samples of a diameter no larger than 5 mm while amorphous steels can be cast with a diameter as large as 16 mm in Fe-(Co,Cr,Mo)-(C,B)-Y system[18]. This reveals the significant role of a suitable amount of C on glass formation of Fe-based amorphous alloys which may be is not sufficient but a prerequisite for producing alloys with critical diameter exceeding 5 mm. Amorphous steels exhibit excellent magnetic and mechanical properties with fracture strengths as high as 4.4 GPa and plastic strain of 0.8% [21]. Amorphous steels containing optimal quantities of chromium are very attractive for practical applications due to their corrosion behavior. These alloys have extraordinary corrosion resistant properties even in hostile environment.

1.3 Glass Formation

The metallic melts, because of their metallic bonding nature, have a high tendency to crystallize while cooling to temperatures below their melting point T_m. Formation of the first nucleus will require at least the time, t_{min}, for all molecules constituting the nucleus to rearrange from the initial disordered liquid state to the final stable crystalline state [22]. When a glass-forming material is cooled with a sufficient high cooling rate (higher than minimum cooling rate required for nucleation) from the equilibrium liquid state, the metallic melt becomes *undercooled* and bypasses the crystallization event. As the temperature of the metallic melt is reduced, its specific volume (or enthalpy) decreases, it becomes more viscous and finally could form a glass. This situation usually occurs for viscosities around 10^{12} Pa·s, so the temperature range at which the viscosity of the undercooled liquid reaches this value is called *glass transformation region*. Figure 1.2 schematically shows the cooling curves for three different cooling rates.

Since the glass transformation region is controlled by kinetic factors, i.e., by the viscosity of the super-cooled melt, there is no unique temperature of glass transition for a given material. The temperature at which the change of slope occurs in *v-T* diagram is called *fictive temperature* (T_f) and to be more precisely defined, is considered as the intersection of the extrapolated liquid and glass curves.

It is seen in Figure 1.2 that a glass produced in a slower cooling rate has a lower T_f. Since it is difficult to study the cooling process of glass forming materials, the *glass transformation temperature* (T_g) values are most

commonly determined upon heating by means of differential scanning calorimetry (DSC) or differential thermal analysis (DTA).

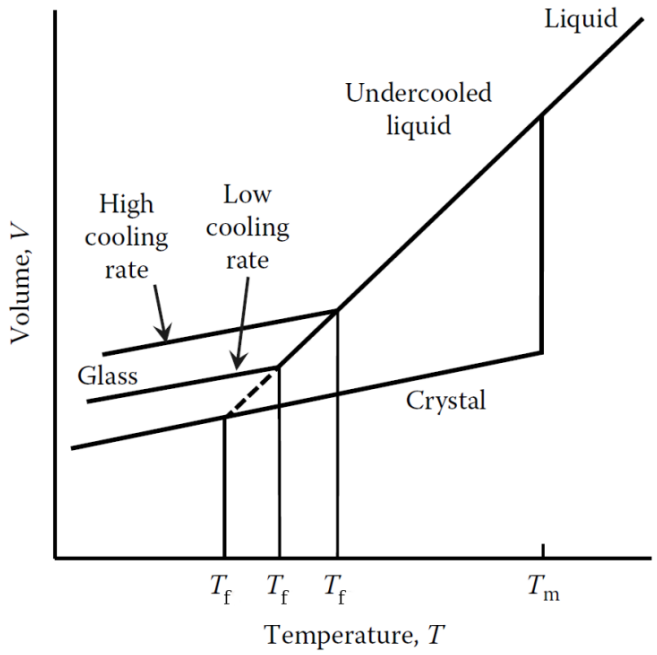

Figure 1.2 Variation of specific volume with temperature of glass-forming and 'normal' crystal-forming materials.

Obviously to have an accurate value of T_g (identical to T_f) , the heating and cooling should be in the same rates and considering the high cooling rates necessary for glass formation and the limited heating rates available in DSC and DTA, it is not easy to obtain a precise T_g for glasses. Despite this, T_g determined during continuous heating with typical heating rates of 10-20 K/min is a good indicator of the approximate temperature where the super-cooled melt converts to a glass.

1.3.1 Glass Forming Ability of liquid alloys

It has been mentioned that glass-forming materials become undercooled when cooled form their liquid state with a sufficiently rapid cooling rate. But what are glass forming materials and why some materials have greater glass forming tendency than others when cooled at the same rate? The easiness to form a glass by cooling the melt is defined as the *glass-forming ability* (GFA). The GFA of a melt can be directly evaluated by the critical cooling rate (R_c) which is the minimum cooling rate necessary to completely suppress crystallization during solidification. A maximum accepted fraction of solid crystalline phase is about 0.0001% to consider a material as a glass. The volume fraction of crystallization, *X*, is given by the equation:

$$X = \frac{4\pi}{3R^4} \int_{T_l}^{T_g} I(T') \left[\int_{T'}^{T_g} u(T'')dT'' \right]^3 dT' \qquad 1.1$$

Where *I* and *U* are the nucleation and growth rates respectively, *R* is the magnitude of cooling rate and *T* is the temperature. The double integral sums over all nucleation centers appearing at T'' and their growth from T' to glass transition temperature, T_g. If the volume fraction of crystals is selected as the maximum allowed fraction for glass formation, then the critical cooling rate, R_c can be derived from Equation 1.1 as

$$R_c^4 = \frac{4\pi}{3 \times 10^{-4}} \int_{T_l}^{T_g} I(T') \left[\int_{T'}^{T_g} U(T'')dT'' \right]^3 dT' \qquad 1.2$$

R_c is usually determined making use of the time-temperature-transformation (TTT) diagram. Figure 1.3 shows a schematic TTT diagram for a liquid alloy that is cooled from above the liquidus temperature T_l, at different cooling rates.

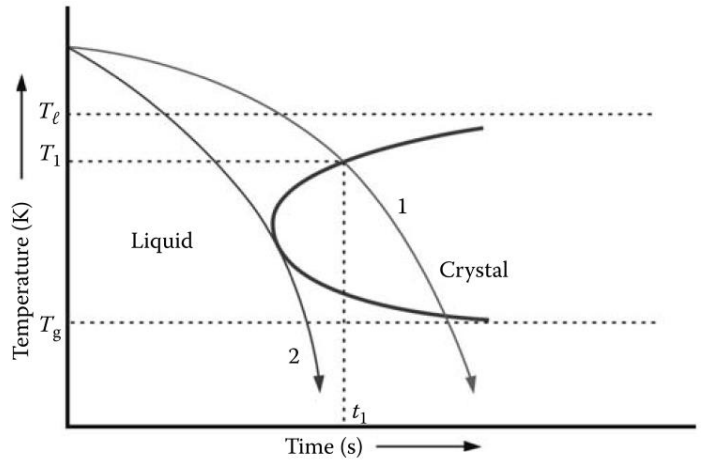

Figure 1.3 Schematic time–temperature–transformation (T–T–T) diagram.

A glass can be formed if the cooling is so fast that the crystallization nose can be avoided (curve 2 of Figure 1.3). Below the glass transition region around T_g the undercooled melt becomes a glass. The glass forming ability of a melt can also be evaluated in terms of the maximum critical thickness attainable (t_{max}) for glass formation. However, it is quite difficult to measure the critical cooling rate precisely, and the critical thickness is strongly dependent upon the fabrication method used. Furthermore R_c and t_{max} can only be determined once the glassy alloy has

been synthesized. Thus significant efforts have been devoted to find other criteria to estimate the GFA in metallic alloy systems.

1.3.2 Glass-Forming Ability Criterion

Since most of glasses are produced by trial and error approaches, estimation of GFA could avoid time consuming laboratory investigations and this is thus a key step to rapid development of new glasses. In 1969 Turnbull [22] identified the *reduced glass transition temperature* (T_{rg}) and now it is one of the most used GFA parameters. This parameter is defined as the ratio of the glass transition temperature and the *liquidus* temperature (T_l).

$$T_{rg} = \frac{T_g}{T_l} \qquad 1.3$$

A low T_l and a high T_g indicate a higher tendency for glass to form and hence a larger value of T_{rg} points out to an easier glass formation.

From classical nucleation theory, a liquid with a high viscosity at high temperatures typically exhibits a high GFA with a low R_c. Since the viscosity at glass transformation region is approximately constant (>10^{12} Pa·s), it was proposed that a high value of the reduced glass-transition temperature, T_{rg}, would result in a high viscosity in the supercooled liquid state, and, consequently, leads to a low R_c. According to the nucleation theory, when $T_{rg} \geq 2/3$, the homogenous crystal nucleation is likely to be suppressed. In other words, the liquid has less time for nucleation of crystalline phases for the same cooling rate when the interval between T_l and T_g is shorter. The metallic glasses with a high GFA are known to have a T_{rg} larger than 0.6.

Although T_{rg} which is obtained from the classical nucleation theory of Turnbull shows an acceptable correlation with $R_{c,}$ many good glass formers show a low T_{rg} [23]. Furthermore, T_{rg} only considers the ease of glass formation of the glass and not the stability of the glassy phase against crystallization.

It is evident that the GFA of a system do not solely depend on the cooling rate and the alloying element, but also on the alloy composition. It has been found that the best glass formation occurs at or near-eutectic compositions [24, 25] where the T_{rg} has the highest value. This empirical criterion can be used for binary and some ternary alloy systems for which their phase diagrams are available. For metal-metalloid systems eutectic compositions are found at around 20 at% metalloid in metal systems. For multicomponent alloys which their phase diagrams are not available, based on confusion principle and solid solution phase formation conditions, Inoue [26] summarized four empirical rules for successful synthesis of BMGs: 1) The alloy should consist of more than three elements, 2) the alloy should contain two or more metallic elements with significant different atomic size ratios (above about 12%), 3) the metallic elements should have large negative heats of mixing with the metalloid type of components and 4) the alloy should be close to an eutectic composition. The super-cooled liquid in the alloy system which satisfies these empirical component rules causes the increase in the degree of dense random packing, which is favorable for suppressing the nucleation of crystalline phase through the increase in liquid/solid interface energy and decrease of atomic mobility.

The super-cooled liquid region (ΔT_x) which is defined by the difference between the onset crystallization temperature (T_x) and the glass transition temperature (T_g), (T_x-T_g), is a criterion for stability of the glassy phase and resistance to crystallization. A large ΔT_x value indicates that the super-cooled liquid can exist in a wide temperature range without crystallization and has a high resistance to the nucleation and growth of crystalline phases [27]. Inoue proposed that the ΔT_x can be used as an indicator of glass forming ability as the critical cooling rate for glass formation decreases with an increase in the ΔT_x value.

In 1970s a new GFA parameter was proposed by Donald and Davis [28]. They argued that the GFA of alloys could be related to the fractional departure of T_m from the rule of mixtures melting temperatures (T_m^{mix}),

$$\Delta T^* = \frac{T_m^{mix} - T_{liq}}{T_m^{mix}} \qquad 1.4$$

Where

$$T_m^{mix} = \sum_i^n X_i T_m^i \qquad 1.5$$

and X_i and T_m^i are the atomic fraction and melting point of the i^{th} component and T_{liq} is liquidus temperature. It was found that most of the glass forming alloys had values of $\Delta T^* \geq 0.2$.

Another parameter, K_{gl}, suggested by Hruby [29] is based on the concept of thermal stability of the glass on reheating to higher temperatures. The Hruby

glass stability parameter is proportional to the ease of glass formation of the melt. K_{gl} is computed as

$$K_{gl} = \frac{T_x - T_g}{T_m - T_x} \qquad 1.6$$

The higher the values of K_{gl}, the higher the stability of the glass against crystallization on heating. Also as the critical cooling rates for glass formation increases the value of K_{gl} decreases.

Although all the parameters discussed above are used as indicators of the GFA for metallic glasses, the trend of GFA in some alloying systems cannot successfully be predicted by these parameters. Thus, more precise criterions were established to reflect the GFA of metallic glasses.

Lu and Liu argued that the criteria indicating the glass formation of the alloys involves a competing process between the liquid and the crystalline solid phases that are formed [30]. These authors discussed that GFA not only refers to the formation of the glass but to the thermal stability of it too. Thus, GFA should include two components:

1) the stability of the liquid phase

2) the resistance to crystallization of the glass

Combining the two above aspects, they proposed a simple GFA indicator $\gamma = T_x/(T_g + T_l)$, which showed more satisfactory correlations with GFA than other GFA parameters proposed before. Figure 1.4 shows the

relationship between the γ parameter and the critical cooling rate (R_c) and the maximum attainable thickness.

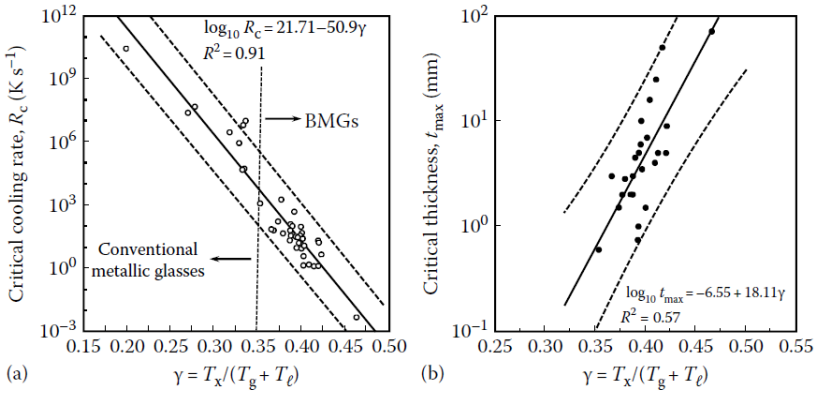

Figure 1.4 Correlation between the γ parameter and (a) critical cooling rate (*Rc*) and (b) the maximum section thickness (t_{max}) for BMGs [5].

A linear relation was observed between γ and $log\ R_c$ and $log\ t_{max}$:

$$\log_{10} R_c = (21.71 \pm 1.97) - (50.90 \pm 0.71)\gamma \qquad 1.7$$

and

$$\log_{10} t_{max} = (-6.55 \pm 1.07) + (18.11 \pm 0.70)\gamma \qquad 1.8$$

Although the γ parameter can be considered as a simple and reliable GFA measure in various known metallic glasses, it was not able to predict the GFA accurately in some alloys systems.

In 2007, Du et al. defined a more precise GFA parameter by considering simultaneously the supercooled liquid range and the γ parameter [31]. These

authors called this new parameter, *modified* γ (γ_m), and claimed that it exhibit a better correlation with GFA even than γ.The γ_m parameter is expressed as

$$\gamma_m = \frac{2T_x - T_g}{T_l} \qquad 1.9$$

A linear regression analysis showed that there is a linear relationship between $\log_{10} R_c$ and γ_m, which can be expressed as

$$\log_{10} R_c = 14.99 - 19.441\,\gamma_m \qquad 1.10$$

Considering the fact that T_l can be a measure of stability of the liquid phase with respect to competing crystalline phases during glass formation and that the thermal stability of the formed glass is closely related to T_x, Mondal and Murty [32] defined a new parameter α:

$$\alpha = \frac{T_x}{T_l} \qquad 1.11$$

This α parameter has the best correlation for Au and Cu based metallic glasses in comparison with other GFA indicators. Also this parameter is very useful to evaluate the GFA of the systems which do not exhibit a distinct glass transition temperature (e.g. in some melt-spun glassy ribbons). For an alloy to have good GFA the value of α should be greater than 1.5.

Based on classical theory of nucleation and growth of the crystalline phase and the perspective of phase transformation kinetics, Chen et al. [33] proposed a new criterion, δ, for evaluating the GFA of amorphous materials. δ is defined as

$$\delta = \frac{T_x}{T_l - T_g} \qquad 1.12$$

This parameter showed the best correlation with GFA in Nd and Pt based metallic glasses among all parameters.

Long et al. [34] developed another criterion: $\omega = T_g/T_x - 2\,T_g/(T_g + T_l)$, to evaluate the GFA of metallic glasses considering both the resistance of amorphous phase against crystallization and the stability of under-cooled liquid against competing crystalline phase formation. They claimed that this new criterion is a better indicator in reflecting GFA than all the parameters in a number of BMG compositions.

Fran et al. employed a model glass-forming system, with a constant melting temperature using the fragility concept and nucleation theory and proposed a dimensionless parameter [35], φ expressed as

$$\varphi = T_{rg}\left(\frac{\Delta T_x}{T_g}\right)^{0.143} \qquad 1.13$$

The relationship between φ and R_c can be expressed by an equation as

$$\log_{10} R_c = (8.638 \pm 0.475) - (18.01 \pm 1.055)\varphi \qquad 1.14$$

The φ parameter has the best correlation for Ce, La, Ni and Fe based metallic glasses in comparison with other GFA indicators.

From the regression analysis of the plots between the various GFA criteria and t_{max}, one could evaluate the statistical correlation factor, R^2. The R^2 value can give an idea of the effectiveness and consistency of different GFA parameters. The higher the R^2 value, the better is the correlation between the proposed GFA parameter and t_{max}. Table I compares the R^2 values for maximum critical diameter, against the different criteria proposed to explain the GFA of Fe-based metallic glasses. These parameters exhibit a very poor correlation with the critical thickness in the case of Fe-based alloys and it is evident that the best correlation was obtained with φ parameter among all the GFA criteria. It is known that GFA is influenced not only by the factors belonging to the glass itself but by the extrinsic factors like inclusion or dissolved impurities in the melt, the initial temperature of the mold during casting etc. [36, 37], so even in the systems with the strong correlations between the GFA parameters and thickness (like Au and Nd-based metallic glasses) [5] not all the parameters can be used to infer GFA [38]. However, despite the poor correlations between the criteria and t_{max} in some cases and the effect of extrinsic factors, these criteria are useful for a rough estimation of the GFA of metallic glasses [30-35].

Table. I The values of statistical correlation factor for Fe-based metallic glasses [5].

GFA Parameters	T_{rg}	ΔT_x	α	β	γ	γ_m	φ	δ	ω
Correlation factor	0.005	0.019	0.012	0.012	0.020	0.025	0.031	0.006	-

1.3.3 GFA of Fe-based metallic glasses

Although metallic Fe-based glasses have been known as an interesting class of engineering materials, their low GFA limits the potential of using them as engineering structural material. Due to their low GFA, the formation of their amorphous phase usually requires cooling rates higher than 10^5 K/s. This high cooling rate limits the production of these materials to thin wires, ribbons, films and a few millimeters diameter rods [39, 40]. Nearly all Fe-based amorphous alloys generally contain 20% of one, or a combination of the metalloid elements like C, B, P and Si [13]. Small metalloid atoms suppress the formation of crystal nuclei by disrupting the short-range order. According to the confusion principle, the increase in the components of the alloy can stabilize the liquid phase by destabilizing the competing crystalline phases which form during cooling [41]. Thus, for improving the GFA the multi-metalloid addition is more effective than the single metalloid addition [42]. The GFA of Fe-based metallic glasses are found to be improved by addition of suitable amount of metalloid additions, while further metalloid addition leads to the precipitation of new crystalline phases during the casting process. Also changing the metalloids content can affect the crystallization onset temperature, leading to change of thermal stability of the alloy [43]. For example metalloids with small atomic size like C or B may make the amorphous structure tighter and then stabilize the amorphous structure against crystallization [44].

Although the important effect of metalloid on GFA and thermal stability of metallic glasses have been reported by many authors [42-44], there are no many reports which systematically compare the effect of different metalloids

versus each other. Although C has a positive heat of mixing with Fe [45] which decreases thermodynamic driving force for glass formation, comprehensive studies of Fe-based metallic glasses show that carbon is the most effective metalloid for glass formation of these alloys. This can be attributed to: 1) the frustration of formation of crystals due to the presence of elements with the combination of positive and negative heat of mixing and 2) the atomic size effect of C [46].

The atomic size of the metalloids change in the order of Si > P > B > C (see table II) so C is the best candidate for atomic size mismatch criteria between metalloids as the atomic radius of C (0.0773 nm) is the smallest and its difference with Fe is the largest.

Table.II Enthalpies of mixing and atomic size mismatch of different metalloids with Fe

	Fe-C	Fe-B	Fe-P	Fe-Si
Enthalpies of mixing (Kj/mol)	+40	-11	-31	-18
Size mismatch with the Fe atom	37.9%	27.4%	12.1%	2.1%

Although casting thicknesses of 16 mm for Fe-Co-Cr-Mo-C-B-(Y or Tm) [18, 47], 12 mm for Fe-Cr-Mo-C-B-(Er or Y)[48, 49] and 10 mm for Fe-Mn-Mo-Cr-W-C-B [47] systems have been reported, most of the Fe-based amorphous cannot be considered as bulk metallic glasses. A variety of elements have been added or substituted into Fe-based BMGs to overcome the poor GFA or further improving their GFA. It was reported that the

addition of small amounts (usually <2 at %) of rare earths, such as Y, Gd, Dy, Ho and Er to the Fe-metalloid alloys improves the GFA in some cases [48]. The enhanced GFA caused by addition of rare earths can be associated to: 1) rare-earth elements (REE) stabilize the liquid phase by forming strongly bonding pairs and filling free volume, 2) addition of large atoms like Y could adjust alloy compositions closer to the eutectics and thus stabilizes the liquid phase, 3) the elimination of heterogeneous nucleation sites by formation of innocuous REE-oxides which act as an oxygen impurity scavenger.

1.4 Corrosion

1.4.1 Introduction to Corrosion

The effect of environment on a material is responsible for many functional failures, so it is crucial to understand the corrosion behavior of new materials in a desired environment and the methods of prevention of different types of corrosion. Corrosion can be categorized in some common types: (1) uniform corrosion, (2) galvanic corrosion, (3) pitting corrosion, (4) crevice corrosion, (5) intergranular corrosion and (6) stress corrosion. Uniform corrosion is the uniform penetration (or thinning) of a metal without any localized attack. For passive metals and alloys, uniform corrosion is rare or only possible in very aggressive environments. Galvanic corrosion occurs when two dissimilar metals or alloys with different electrochemical potentials are in contact in a corrosive media. In fact the difference of potential between the metals is the driving force for corrosion initiation. Pitting is a localized corrosion by which sharply defined holes are produced in the materials that have protective films. It is often difficult to detect pitting corrosion because the corrosion products mask them. Crevice corrosion which is also known as contact corrosion is another type of metallic localized corrosion form which is initiated by the extremely low availability of oxygen due to close proximity of another metal or nonmetallic surface. Intergranular corrosion is defined as the dissolution at or adjacent to grain boundaries, without appreciable attack of the grains themselves. Finally, stress corrosion is due to the combined effect of tensile stress and corrosive environment. In general, a

mechanism of corrosion is the actual atomic, molecular, or ionic transport process that takes place at the interface of a material.

1.4.2 Corrosion mechanisms

The general corrosion mechanism involves at least two partial reactions in anode and cathode. In the anodic reactions the metal is oxidized (corroded) to a higher valence state. The oxidation reaction can be expressed as follows:

$$M \rightarrow M^{z+} + ze^{-}$$

Where z is the valence of the metal ion.

The cathodic half-reactions are more difficult to predict but depending on the PH and the availability of oxygen in the medium (solvent), can be categorized into one of three different types of reduction reactions:

1. Evolution of Hydrogen:

$2H^{+} + 2e^{-} \rightarrow H_2 \uparrow$ (in acid solutions)

$2H_2O + 2e^{-} \rightarrow H_2 \uparrow + 2OH^{-}$ (in neutral and alkaline solutions)

upward arrow indicates a gas (hydrogen bubbles).

2. Reduction of dissolved oxygen:

$O_2 + 4H^{+} + 2e^{-} \rightarrow 2H_2O$ (in acid solutions)

$O_2 + 2H_2O + 4e^{-} \rightarrow 4OH^{-}$ (neutral and alkaline solutions)

3. Reduction of a dissolved oxidizer in a redox reaction:

$M^{3+} + e^{-} \rightarrow M^{2+}$ (Metal ion reduction)

$M^{2+} + 2e^{-} \rightarrow M$ (Metal deposition)

These reactions proceed to the right (i.e., corrosion actually occurs) if there is a negative free energy change *(*ΔG).

An electrochemical cell is a device or a mechanism which can be created by placing metallic electrodes into an electrolyte where a chemical reaction either uses or generates an electric current. Electrochemical cells can operate either as *galvanic cells*, in which chemical reaction occur spontaneously and chemical energy is converted into electrochemical energy, or as *electrolytic cells*, in which electrical energy is converted into chemical energy.

For electrochemical reactions, the free energy change is calculated from the well-known relation:

$$\Delta G = -nFE \qquad 1.15$$

Where *n* is the number of participating electrons, *F* is Faraday's constant (9.648×10^{4} C mol^{-1}), and *E* is the *cell potential* which is the potential difference between the two half cells. The negative sign in this equation shows that the cell acts as a source of energy. In electrolytic cells the potential of the working electrode is compared to a reference electrode which is practically at equilibrium. When two partial reactions occur simultaneously on a metal surface, both of them will change the potential (with respect to the reference electrode) to an intermediate value called the *corrosion potential*. At the corrosion potential the rate of oxidation is equal

to the rate of reduction, consequently anodic and cathodic currents (i_a and i_c) are equal but opposite so the net reaction rate is zero ($i=i_a+i_c=0$).

When the cell is not polarized by the application of any external voltage, it is in the equilibrium state and the potential in this state is called the *equilibrium potential* E_{eq}. The equilibrium potentials are governed by Nernst equation which relates the cell potential to the potential of the cell under standard conditions (298 K, 1 atm, and 1.0 M) (E^0) and to the concentration of oxidized (C_{ox}) and reduced (C_{red}) species by the following equation:

$$E_{eq} = E^0 - \frac{RT}{nF} ln \frac{C_{ox}}{C_{red}} \qquad 1.16$$

The partial current density of each reaction obeys the Butler-Volmer equation:

$$i = i_a + i_c = i_0 exp\left[\frac{\eta}{\beta_a}\right] - i_0 exp\left[-\frac{\eta}{\beta_c}\right] \qquad 1.17$$

Where η is the overvoltage, the difference between the potential imposed on the specimen and the corrosion potential, and β_a and β_c are the anodic Tafel constant:

$$\beta_a = \frac{RT}{\alpha nF} \qquad 1.18$$

and the cathodic Tafel constant,

$$\beta_c = \frac{RT}{(1-\alpha)nF} \qquad 1.19$$

Where α is the transfer coefficient which gives the fraction of the potential difference that influences the forward reaction. The values of anodic (βa) and cathodic (βc) Tafel constants are measured from the anodic and cathodic slopes respectively (figure 1.5).

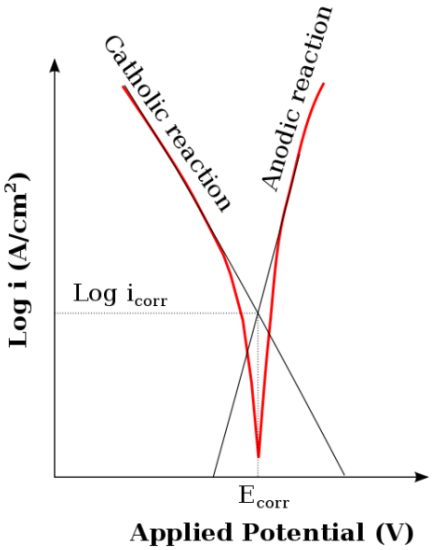

Figure 1.5 Corrosion Process Showing Anodic and Cathodic Current Components.

The Anodic Tafel region is the region of potential where η is small compared to β. For the anodic direction, Equation 1.17 yields:

$$i = i_a = i_0 exp\left(\frac{\eta}{\beta_a}\right) \qquad 1.20$$

Where i_0 is the exchange current density

And taking the logarithm gives:

$$\eta_a = -\beta_a ln i_0 + \beta_a ln i \quad 1.21$$

This equation can be written as,

$$\eta_a = a_a + b_a log i \quad 1.22$$

Where a_a and b_a are the anodic Tafel constants:

$$a_a = -2.303\beta_a log i_0 \quad 1.23$$

$$b_a = 2.303\beta_a \quad 1.24$$

For the cathodic Tafel region, $\eta/\beta_c \ll -1$, and equation 1.17 is simplified to the following form:

$$i = i_c = -i_0 exp\left(-\frac{\eta}{\beta_c}\right) \quad 1.25$$

$$\eta_c = \beta_c ln i_0 - \beta_c ln|i| \quad 1.26$$

Similar to anodic Tafel constants, cathodic Tafel constants a_c and b_c of the Tafel equation of a cathodic reaction can be expressed as:

$$\eta_c = a_c - b_c log|i| \quad 1.27$$

$$a_c = 2.303\beta_c log i_0 \quad (1.28)$$

$$b_c = 2.303\beta_c \quad (1.29)$$

According to these equations, the corrosion rate i_{corr} can be obtained by extrapolating back to the corrosion potential E_{corr} of the anodic and cathodic Tafel lines because $i=i_{corr}$ when $\eta=0$.

1.4.3 Factors influencing corrosion

There are several factors controlling the behavior of corrosion. In the case of metals and metal alloys these factors include: 1) nature of the material, 2) nature of the corrosion product and 3) nature of the corroding environment.

The corrosion behavior of materials varies markedly depending on the alloying elements. The corrosion resistance of more reactive materials can be significantly improved by adding even a small amount of a more corrosion resistant component (e.g. Cr, Al and Ni) [50, 51]. For example, iron–chromium alloys containing 13% chromium can survive in aggressive environment for a long time, whereas pure iron corrodes quickly [52]. Although elemental alloying can affect the corrosion resistance in many different ways, including dissolution kinetics, phase structures and the ability to catalyze the cathodic half-reaction parameters, the main purpose of adding corrosion enhancer elements is forming thin passive-film on the surface of the metal or alloy underneath. This thin protective film can be

formed by a small addition of passive elements. Smaller quantities of adding elements are desirable because they do not bear an adverse effect on other properties.

The corrosion behavior is highly sensitive not only to compositional but to structural features of the material which may change the thermodynamic activity of the surface and thus dramatically affect the corrosion resistance [53, 54]. Even extremely pure single crystals have defects which can act as nucleation site for corrosion. In crystalline materials structural defects like grain boundaries, second phases, inclusions and impurities often have detrimental effect on corrosion resistance. For alloys with a microstructure of more than two phases, there can be significant galvanic action among the different phases. For example, corrosion rate of dual-phase steels (dual phase refers to existence of ferrite and martensite phases) depends upon the volume fraction and morphology of the phase constituents [55]. As another example, the formation of carbides at grain boundaries of stainless steel deteriorates the corrosion resistance through the formation of susceptible Cr-depleted zones in neighboring matrix [56]. This negative effect on corrosion resistance can be diminished by heat treatments [57].

1.4.4 Corrosion of Amorphous materials

Metallic glasses are known to often have excellent corrosion resistance even under extremely severe corrosion environments [58, 59]. This excellent corrosion behavior is promising to industrial type applications that require long-term performance [60, 61]. The reason for their good corrosion resistance comparing to their crystalline counterparts has been explained in

terms of their structural and chemical homogeneity and lack of heterogeneities such as grain boundaries, dislocations, second phases and segregates typically found in crystalline materials. Also the glassy alloys high anodic reactivity leads to a rapid enrichment of film-former elements in the protective film.

From the theoretical point of view, when a reaction is anodic the second term in the Butler-Volmer equation (1.17) becomes negligible and the exchange current density of the metal charge transfer reaction, i_0, can be expressed by equation (1.20)

The dissolution rate is therefore a function of the exchange current density which is in turn given by [62]

$$i_0 = nvF\alpha(\frac{N_s}{N_0})\exp(-\frac{\Delta G^*}{RT}) \qquad 1.30$$

Where, v is a frequency factor (about 10^{12} sec^{-1}), α the fraction of active surface atoms, N_s the number of atoms per unit surface area (about 10^{15} cm^{-2}), N_0 Avogadro's number and ΔG^* is the electrochemical free energy of activation. The featureless uniform surface of a glassy alloy brings smaller α when compared to its crystalline counterpart. However, since the amorphous phase is a metastable phase, it may be expected to have a smaller ΔG^*. Therefore both these factors should be considered to see which one is dominant. Although the amorphous structure is thermodynamically metastable and their surface requires very small activation energy for chemical reactions, high solid/electrolyte interfacial free energy and chemically homogeneous nature of these materials provide high passivating

ability leading to an adherent layer which separates the metal from the environment. The noncrystallinity of the defect free protective film formed on amorphous materials is also an important reason of enhanced corrosion resistance in amorphous materials [63].

1.4.5 Corrosion of amorphous Fe-based alloys

During the last decades the Fe-based metallic glasses have been successfully applied in the corrosive environments so a great deal of effort has been made to understand the interaction of these high corrosion resistant alloys with their environment.

The high corrosion resistance of Fe-based amorphous alloys has been reported in various reports since 1974 when Naka et al. studied the corrosion behavior of Fe-based alloys with Cr, P and C in acidic solution [64]. Figure 1.6 shows the corrosion rates of amorphous Fe-10Cr-13P-7C alloy versus crystalline type 304 stainless steel (Fe-18Cr-8Ni) in different concentrations of hydrochloric acid (HCl) at room temperature.

It can be seen that the amorphous Fe-10Cr-13P-7C alloy was not corroded even in 1 M HCl while the crystalline type 304 stainless steel with higher Cr content is not resistant to hydrochloric acid at any concentration. The high corrosion resistance of Fe-Cr-P-C amorphous alloy was due to the homogeneous single-phase nature of the sample and the oxide film which covered uniformly the sample without having any heterogeneity.

Although in amorphous structure there are no sites for preferential corrosion attack, only amorphous alloys with sufficient concentrations of beneficial elements show superior corrosion resistance [65].

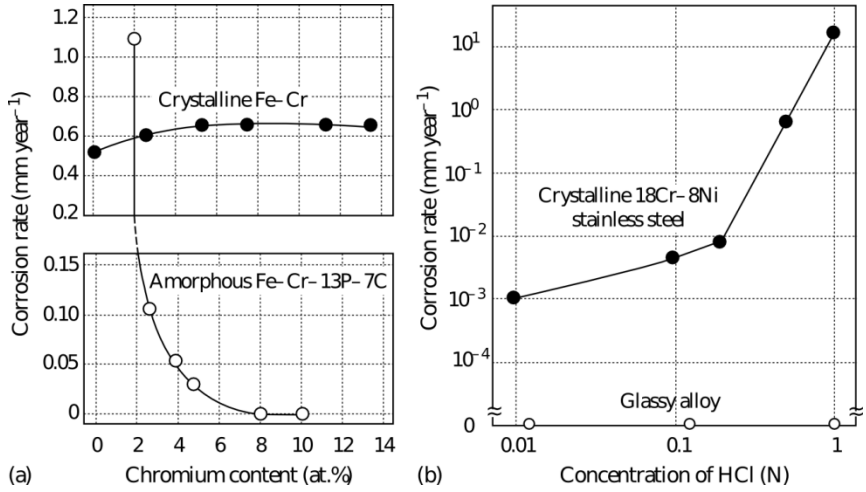

Figure 1.6 Corrosion rate of the $Fe_{80-x}Cr_xP_{13}C_7$ amorphous alloy and crystalline Fe-Cr alloy plotted versus chromium content (a) and concentration of HCl (b) [64].

In section 1.2 it was mentioned that in the Fe-based amorphous alloys the presence of a large quantity (≅20 at.%) of the metalloid elements is required to form the amorphous structure. The corrosion resistance of binary iron-metalloid amorphous alloys is known to be significantly lower than that of crystalline pure iron. However, amorphous Fe-metalloid alloys were found to have an improved corrosion resistance with the addition of second metallic elements like Cr, Mo, Ni and Zr [66, 67].

The different metalloids (P, B, Si, C) show drastically different effects on the corrosion resistance of the alloys depending on the major constituent elements and corroding agent [42, 68, 69]. It is known that P is the most effective metalloid element for improvement of the corrosion resistance of Fe-Cr alloys. Fe-based metallic alloys have attracted huge interest mainly owing to their excellent magnetic properties, but as Fe-based amorphous

alloys containing large amount of P are not successful candidates for potential magnetic application, P addition is not suggested as a corrosion inhibitor in these alloys. The role of C and B metalloids as a corrosion inhibitors are also reported by several authors [69, 70] but they may have a detrimental effect on corrosion resistance by forming chromium-(carbide/boride) and, as a consequence, reducing the amount of chromium available to ensure corrosion resistance in Cr-depleted areas.

1.4.6 Active-Passive behavior

Figure 1.7 schematically presents the current-potential plot of an active-passive type metal which has undergone passivation during a potentiodynamic test. The first part illustrated in the figure is the *active* region, in which the anodic dissolution rate increases as the applied potential is made more positive.

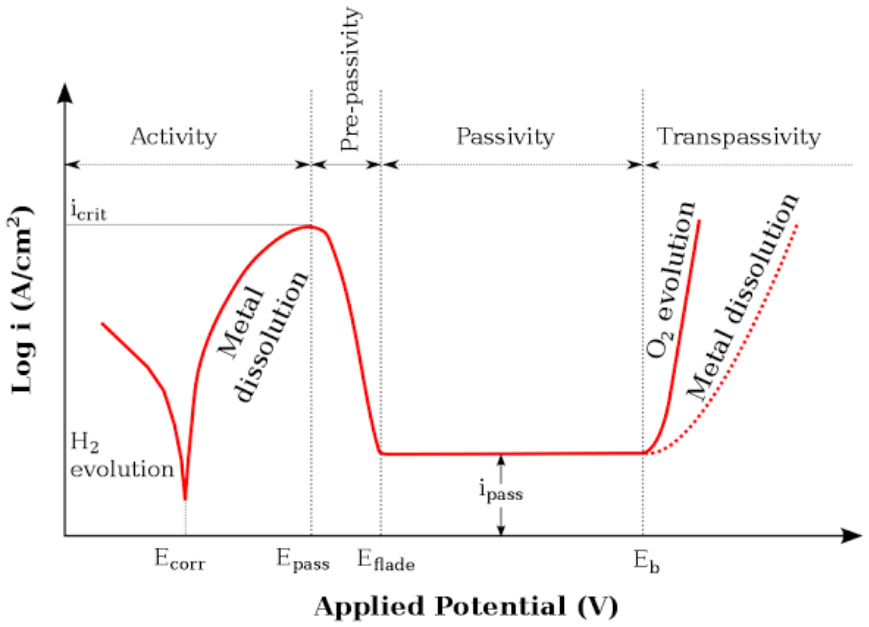

Figure 1.7 Schematic current -potential plot for an active passive type metal, showing active, passive and transpassive region.

A linear increase is observed until the onset of *passivation* begins at higher potentials (becomes more oxidizing). In *pre-passivaion* region as the potential increases an abrupt drop to small values of corrosion current is

observed. This sharp decrease in current corresponds to the decrease in the surface of the metal chemical reactivity, probably due to the formation of a passive protective film on the surface of the metal. The current density and potential at which the fall occurs are referred to as the critical current density i_{crit}, and the passivation potential E_{pass}, respectively. Lower values of i_{crit} and E_{pass} indicate higher passivating ability. The potential at which the current degradation stops and reaches a minimum (passive current i_{pass}) is called *flade potential*, E_{flade}. Lower values of E_{flade} and i_{pass} indicate greater stability of the passivating film. Within the passive range, the corrosion current stays in low values independently of the potential until the current eventually rises due to passive film breaking down in the *transpassive* range. The potential corresponding to the end of passive region is referred to *Breakdown potential* (E_b). In E_b passive film dissolves either globally, i.e. transpassive dissolution, or locally, i.e. pitting. The pitting is usually accompanied by a sharper increase in the current than the one for metal dissolution. It is evident that E_b is a representative of the resistance of the passive film against breaking down.

2 Objectives

Generally, Chromium is added to amorphous steels to promote corrosion resistance [64]. All the amorphous steels compositions studied so far for their corrosion resistance have a relatively large amount of Cr (above 7.5 at% in some cases and above 15 at% in most of the cases) [65, 69] and one consequence is the reduction of the GFA. In this study we explore the low Cr range of these alloys, from 0 to 15 at% in order to assess which was the minimum amount of Cr needed to have good corrosion resistance in different environmental conditions while maintaining a good glass forming ability. Also mechanical properties of metallic glasses are highly sensitive to composition change. So the effect of Cr-addition on mechanical behavior was also discussed in order to determine the optimal amount of Cr needed to obtain a composition with environmental stability, good mechanical properties and high glass formability.

The chemical properties of metallic glasses are closely related to their unique amorphous structure [66]. The resistance to pitting and uniform corrosion exhibited by certain glassy alloys is lost in most of the cases if the alloys are structurally changed (relaxed or crystallized) by thermal annealing. Fully understanding the corrosion resistance of these materials and their composites requires investigation of the microstructural changes and their interaction with the corrosion behavior. To achieve this aim a detailed study has been done on the corrosion and passivation behavior of different structural states, i.e. amorphous, relaxed, partially and fully crystallized, obtained by controlled heat treatments of the Fe-based amorphous alloy.

3 Experimental

3.1 Alloy preparation

An amorphous steel alloy with a nominal composition of $Fe_{65-x}Cr_xMo_{14}C_{15}B_6$ (x=0, 2, 4, 6, 8 and 10 at. %) was used in this study. The Fe–Cr–Mo–C–B system is widely studied due to its high GFA and corrosion resistance in aggressive solutions [42]. The addition of Cr to amorphous steels benefits its corrosion resistance but it also affects the GFA, thermal stability and the mechanical response [21]. For instance, the ability to sustain plastic strain is negligible for Cr contents above 10 at.%. However, all the amorphous steels compositions studied so far for their corrosion resistance, have a relatively large amount of Cr (above 7.5 at% in some cases and above 15 at% in most of the cases). In this thesis we explore the low Cr range of these alloys, from 0 to 10 at% in order to fill the gap in the literature and assess the minimum amount of Cr needed to develop a corrosion protective film without losing the high thermal stability, GFA and relatively good mechanical performance.

Master alloys were prepared by arc melting the mixture of constituent elements under a Ti-gettered Ar atmosphere. The purity of the elements was 99.95% for Fe, 99.95% for Cr, 99.95% for Mo, 99.98% for C and 99% for B. In this thesis, these compositions will be referred as Cr0, Cr2, Cr4, Cr6, Cr8 and Cr10 respectively. The arc melting was performed in a Buehler MAM-1 arc melting system. The ingots were turned over and re-melted several times to promote the homogeneity. From the master alloys, amorphous samples were prepared in ribbon shape in an Ar atmosphere with purity of 99.9% by

rapid solidification in a Buehler Melt Spinner SC device. The thickness of the ribbons was ~40 μm and the width between 1-2 mm. The as-quenched ribbons were stored at room temperature and ambient atmosphere.

3.2 Thermal characterization

In order to thermally characterize the ribbons, high temperature DSC (HT-DSC) was performed at a heating rate of 20 K/min. The glass transition temperature (T_g), the onset temperature of the first crystallization event (T_x), the solidus temperature (T_m) and the liquidus temperature (T_l) were determined using a NETZCH DSC 404F3 DSC under protection controlled atmosphere of N_2 gas (flow rate: 50 mL/min). Figure 3.1 shows a typical DSC trace of a metallic glass. In a DSC the differences in heat flow to the sample and a reference at the same temperature is recorded as a function of temperature.

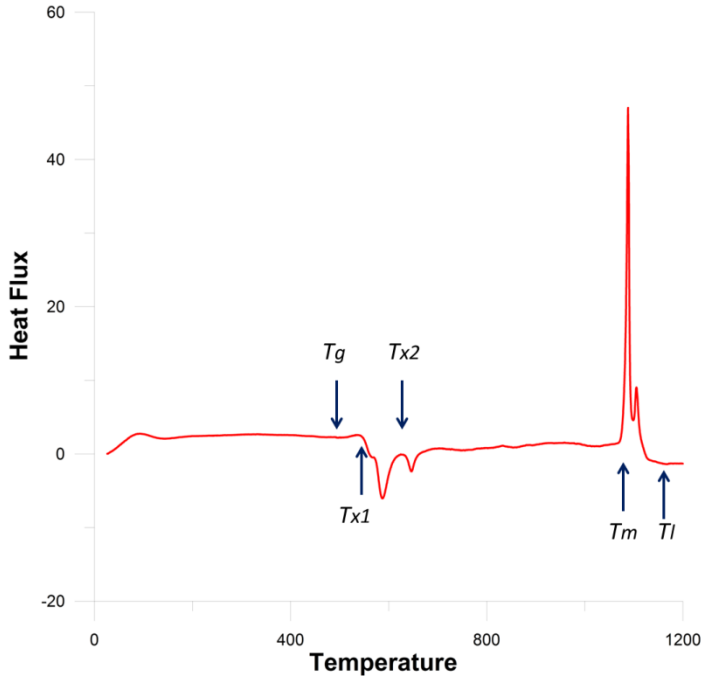

Figure 3.1 DSC curve of Cr0 showing the glass transition, crystallization and melting regions.

Each change in the heat flux indicates a transformation in the alloy. The first transformation is at the glass transition temperature which causes a baseline shift by increasing the heat capacity. The *glass transition temperature* (T_g) is usually regarded as the onset of this change in the plot. The exothermic reaction prior to T_g is a result of the annihilation of free volume during structural relaxation. The exothermic heat is proportional to the amount of escaping free volume and, subsequently, to the increase in the density. On further heating, the alloy gains enough thermal energy for activating nucleation and growth of crystalline phases. The crystallization(s) event is indicated by a typical exothermic process and the point at which this begins is called the (onset of) *crystallization temperature* (T_x). Using the concept of variation of crystallization peak temperature (T_p) with heating rate (β), the activation energy, E_A, of crystallization can be determined by non-isothermal Kissinger analysis [71]:

$$ln\left(\frac{T_p^2}{\beta}\right) = \frac{E_A}{RT_p} + const \qquad 3.1$$

Where, *R* is the gas constant.

The last transformation corresponds to the melting of the sample and is defined by T_m, and is noticed by a large endothermic peak. The temperature at which the endothermic peak re-joins the base line is called *liquidus temperature* (T_l).

3.3 Heat treatment

Heat treatments of the composition with the highest thermal stability of the series [72] (it will be shown in next sections that this corresponds to Cr4) were performed in order to study the microstructure and corrosion behavior of the amorphous, partially crystalline and fully crystalline states of this alloy. The as-quenched Cr4 ribbons were heat treated at 400°C, 500°C, 550°C, 580°C, 600°C, 650°C and 800°C for 20 minutes. These temperatures were selected to completely cover the range between structural relaxation and complete crystallization obtained by DSC. In order to protect the samples from oxidation, all samples were encapsulated in a quartz capsule filled with argon. Before the samples were introduced, the temperature of the furnace was ramped from the ambient temperature up to the desired holding temperature. After the annealing period, the samples were removed from the furnace and allowed to cool down to room temperature before the ribbons were removed from the capsule.

3.4 X-Ray Diffraction (XRD)

In XRD technique an x-ray source projects a collimated beam onto the area of the specimen. When the beam encounters the examined specimen, it is either transmitted, absorbed, refracted, scattered or diffracted. In crystalline materials the distances between the planes of the atoms that constitute the sample can be measured by detecting and processing the diffracted beam signal, applying Bragg's law. Bragg's law refers to the simple equation:

$$n\lambda = 2dsin\theta \qquad 3.2$$

Where *n* is an integer number of wavelengths for constructive interference, λ is the wavelength of the x-ray beam, *d* is the distance between the planes of atoms and Θ is the angle of incidence of the x-ray beam. Using interatomic distances XRD can identify the constituent phases by comparison with data from known structures. For an amorphous structure where there are no planes of atoms and atoms are distributed with lack of periodicity in 3D space, scattered X-rays will show a large bump distributed in the range of scattering angle (2Θ) . In crystalline materials due to the periodic arrangement of atoms the x-rays will be scattered only in certain directions leading to several sharp, well defined peaks.

The amorphous nature and microstructure analysis of as-produced and heat treated samples, respectively, were investigated by x-ray diffraction (XRD). XRD measurements were performed on a monochromic (Bruker AXS D8) using Cu-K_α radiation source (λ=1.5405$\mathring{A}$). Samples were scanned in the 2Θ range of 10° to 110° with a step size of 0.05°.

3.5 Scanning Electron Microscopy (SEM)

When high energy incoming electrons are focused on the surface of solid specimens, they can supply some energy to the *atomic* electrons that are present in the solid, which can then be released as *secondary electrons*. A SEM based on the emission of secondary electrons, generates 2D images with collecting and subsequently processing the signals. These images reveal information about the morphology and microstructure of the sample surface.

A Leo 1550 VP scanning electron microscopy (SEM) was used for the evolution of microstructure and the corrosion morphology examination of

the samples. The acceleration voltage was 6-10 kV and all the images were done at a working distance of 2-10 mm. All the images were taken with the beam energy of 15 keV using secondary electron. SEM was linked to an Energy Dispersive X-ray (EDX) system (*Oxford*) to analyze the composition of the specimens. In the case of corrosion behavior studies in order to remove the corrosion products from the surface, prior to the SEM investigation, the specimens were washed in distilled water and dried.

After nanoindentation measurements, deformation zones of the ribbons were examined using a Joel JSM-6300 SEM. Since the hardness values were impressively high, we have verified that the results are reasonable using the SEM images of the indentation imprints.

3.6 Transmission Electron Microscopy (TEM)

In a Transmission Electron Microscopy (TEM) a coherent beam of high energy electrons with a penetration depth larger than the sample thickness is directed onto the sample. These energetic electrons are partly transmitted through, and partly scattered from the sample. The interaction of the electrons with the sample is detected and magnified to produce very high resolution images. These high resolution images can provide helpful structural information in an atomic level. Also using the diffraction mode of the TEM it is possible to observe the diffraction patterns of different crystal structures. In amorphous materials because of the lack of long-range atomic order, the beam is diffracted over a wide range of angles resulting the selected area electron diffraction (SAED) pattern in the form of a diffuse halo ring.

In this work, High resolution Transmission Electronic Microscopy (HR-TEM) were performed at 200-kV in a Jeol JEM-2200FS equipped with Jeol EDX system and nanobeam electron diffraction (NBD) that allow us to take diffraction patterns from nm-sized regions. SAED technique, bright field (BF) and dark field (DF) imaging were employed to characterize the microstructure and structural analysis. Elemental compositions were provided by Electron energy loss spectroscopy (EELS) via HR-TEM in scanning mode. Thin foils of the samples for TEM were prepared by double jet electro-polishing (Struers Tenupol 5) at 54 V in a solution of 950 ml acetic acid and 50 ml perchloric acid at 15 ºC.

3.7 Electrochemical setup

Electrochemical measurements were done using a three electrode cell with an Ag/AgCl reference electrode and a carbon counter electrode. The working electrode was exposed to an area of 1 cm^2.

With the increased utilization of amorphous steels in practical applications, one of the major problems encountered is the control of corrosion rate when exposed to different corrosive environments. In order to cover the potential applications' conditions, the amorphous ribbons were exposed to electrolytes with different pH values.

Therefore, anodic polarization curves were measured potentiodynamically in three different corrosive media (0.1 N H_2SO_4, 0.1 N HCl and 0.1 N NaCl) at room temperature and pressure with a sweep rate of 2 mV s^{-1}, after immersion of the specimens for 15 min until the open-circuit potentials (OCP) became almost steady. In order to have a high reliability of the

results, all electrochemical measurements were repeated five times. Polarization tests were additionally performed close to the breakdown potential for 1000 s in the H_2SO_4 electrolyte. Prior to any electrochemical and mass loss test, all samples were ion milled for 5 min to remove the surface oxide layer in a Gatan Co., Model 682 PECS with Ar ions at 5 keV and tilting angle of 70°.

The corrosion rates were estimated from the weight loss after immersion in 6 N H_2SO_4 solution open to air at 298 K for 168 h. The electrolytes used were prepared from reagent grade chemical and distilled water. After the immersion tests, the specimens were washed in distilled water, dried, and subjected to weight loss measurement.

3.8 Nanoindentation

Nanoindentation tests were carried out by employing a Nano indenter XP from UMIS Instruments. All experiments were performed at room temperature using three-sided pyramidal Berkovich tip (of diamond) for the characterization of all the ribbons. The maximum value of applied load was 50 mN to ensure that the lateral size of indentation imprint is such that it is significantly more than the surface roughness but smaller than the ribbon thickness to ensure that there is no substrate effect. In order to have high reliability of the results, 25 indentation were performed on the cross section of all the ribbons. The loading and unloading rates were kept constant at 0.25 mN/s for all the nanoindentation tests. The thermal drift was kept below

±0.05 nm/s for all the indentations. Proper correction for the contact area (calibrated with a fused quartz specimen), instrument compliance, and initial penetration depth were applied. Prior to nanoindentation the specimens were carefully polished so that the indentation face was flat and horizontal.

4 Results and Discussion

4.1 Structural Characterization

4.1.1 Amorphous phase

Figure 4.1 shows the X-ray diffraction patterns of the melt-spun ribbons. The XRD patterns show only one broad peak in the 2θ range between 40 and 50º and no diffraction peak corresponding to a crystalline phase is seen for all the alloys as the figure illustrates. All samples are thus in a fully amorphous state.

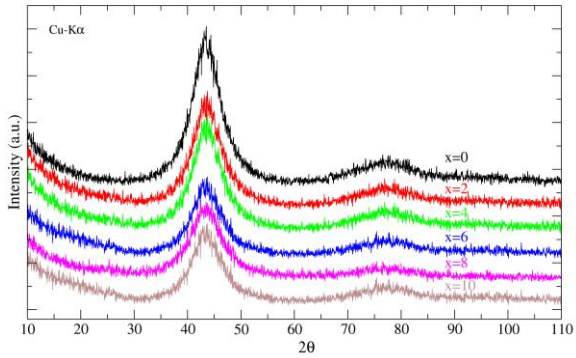

Figure 4.1 XRD patterns of melt-spun ribbons.

Also, Scanning Electron Microscopy (SEM) observations of the as-cast ribbons revealed uniform, featureless surface, which indicate the amorphous nature without detectable crystalline phases of these alloys. Figure 4.2 shows SEM micrographs of the surface of *x*=0, 2, 4, 6, 8 and 10 alloys.

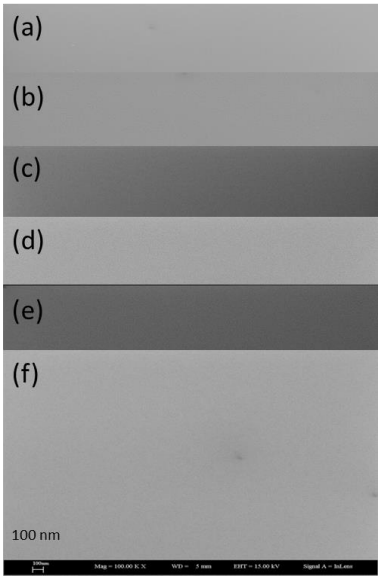

Figure 4.2 SEM micrographs of the surface of As-produced ribbons (a) Cr0, (b) Cr2, (c) Cr4, (d) Cr6, (e) Cr8 and (f) Cr10.

The amorphous structure in the as-quenched Cr4 ribbon was investigated and confirmed by the high-resolution TEM imaging and the selected area diffraction (SAD) pattern, shown in figure 4.3. The bright filed (BF) TEM image shows the typical salt- and-pepper like contrast for amorphous structure. The corresponding SAD pattern reveals diffuse and broad electron diffraction rings without crystalline reflections.

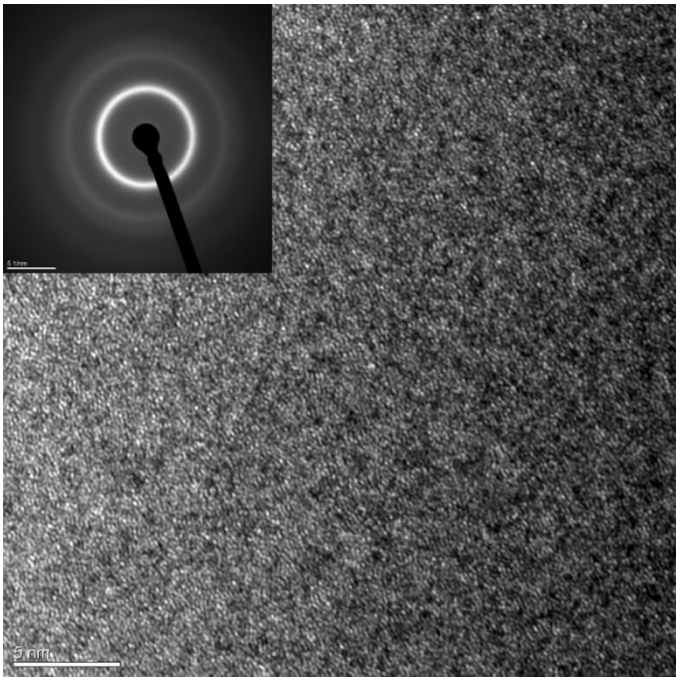

Figure 4.3 TEM images and SAD pattern of Cr4-alloy as-produced.

4.1.2 Structural transformation

The properties of metallic glasses result from their amorphous structure. Due to the frozen-in disorder, the amorphous structure is thermodynamically unstable and tends to undergo structural relaxation, phase separation or transform into crystalline phases which are thermodynamically more stable. This transformation to a lower level of free energy occurs at high enough temperature and/or given long enough time. These transformations may have detrimental effects on desirable properties while they change the random atomic structure of the glass. On the other hand, some properties of

amorphous materials are improved through purposely thermally induced transformations including structural relaxation and crystallization. Structural relaxation can be defined as the moderate structural change of an amorphous phase resulting in a change of density and other properties like viscosity. Unrelaxed amorphous alloys contain an inherent amount of free volume frozen in the glassy structure during the fabricating process [73]. Heating up to the glass transformation range reduces this excess free volume in amorphous alloys and as mechanical, physical and chemical properties are strongly sensitive to the amount and distribution of free volume, the structural relaxation may result in either degradation or upgrade of these properties. For instance, a decrease in the free volume generally increases the hardness and elastic modulus but deteriorates the ductility [17, 74]. Also the ideal glassy state formed by structural relaxation exhibits better corrosion resistance than unrelaxed glassy state [75] because free volume, as a vacancy-like defect, can act as corrosion initiation site.

Metallic glasses crystallize when heated up to temperatures near to their crystallization temperature. Crystallization may happen below the T_x determined by thermal analysis because T_x is not a thermodynamic parameter (like T_l) and is a function of the heating conditions: heating rate, time period that the sample spends at a specific temperature (in isothermal heat treatment process) and in general to its thermal history. So the crystallization of metallic glasses can occur at temperatures even much lower than T_x. Thermally activated crystallization of metallic glasses regardless to its mode (polymorphous, eutectic or primary) involves nucleation and growth [5]. Depending on temperature, nucleation and growth rates, the glass can be

transformed to glassy/crystalline composite, nanocrystalline (with grains size less than 100nm) and polycrystalline materials. Partial or complete crystallization, just like the structural relaxation, is one of the common strategies to enhance/modify the structural properties of metallic glasses.

Figure 4.4 shows the DSC curves of Cr0, Cr2, Cr4, Cr6, Cr8 and Cr10 glassy alloy ribbons.

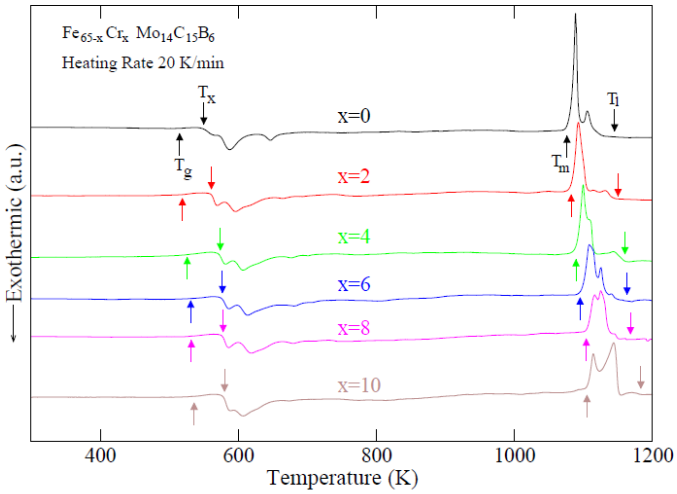

Figure 4.4 DSC curves of $Fe_{65-x}Cr_xMo_{14}C_{15}B_6$ alloys at a heating rate of 20K/min.

As the temperature ramps up, all the samples exhibit a glass transition (T_g), followed first by a super-cooled liquid region (ΔT_x) of 35-48K and then by multistage crystallization. The crystallization processes observed by DSC are similar in all compositions but regularly shifted to higher temperatures by the

addition of Cr. Figure 4.5 also summarize the information obtained from the DSC curves for all the compositions, showing the changes in glass transition, onset of crystallization, melting and liquidus temperature.

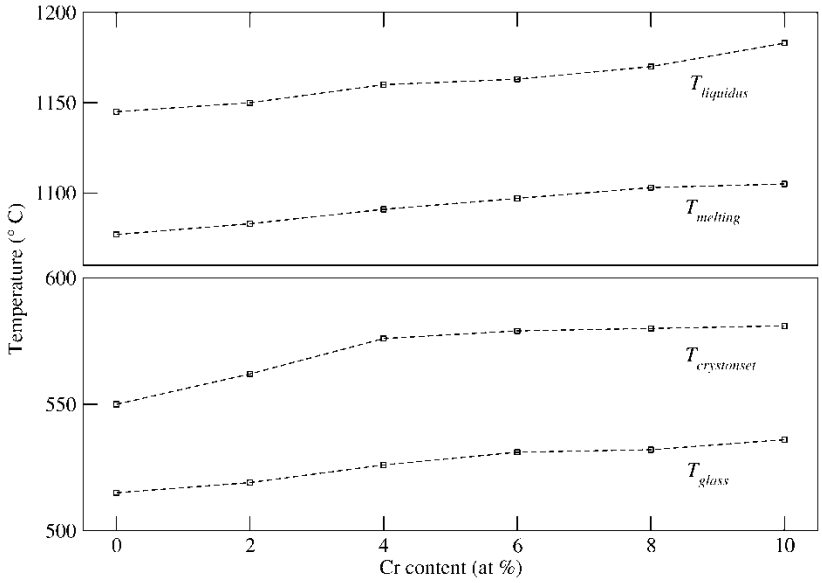

Figure 4.5 Evolution of glass transition, onset of crystallization, melting and liquidus temperatures with Cr addition.

4.1.3 Glass formation

4.1.3.1 Glass forming ability of the Fe-Cr-Mo-C-B system

In 2001, Pang et al. [40] succeeded to form amorphous ribbons of Fe-Cr-Mo-C-B alloy with nominal composition of $Fe_{43}Cr_{16}Mo_{14}C_{18}B_5$. This glassy alloy with high corrosion resistance satisfies the empirical rules for glass formation and exhibits a wide ΔT_x reaching 58K and high T_{rg} up to 0.62. These authors replaced 2% of C by Nb and Ta to improve the corrosion resistance of this glassy alloy but noticed these minor alloying not only do not improve the GFA but decreases the thermal stability of this alloy. Further studies have been done to improve the GFA and thermal stability of Fe-Cr-Mo-C-B system by minor additions of different elements. Replacement of Fe by B could improve thermal stability of $Fe_{50-x}Cr_{16}Mo_{16}C_{18}B_x$ while did not improve the GFA significantly [42] . The same group added small amount of P to Fe-Cr-Mo-C-B system to further improve the corrosion resistance of this alloy and observed that this element is also effective to increase the maximum diameter [69]. Also, they studied the effect of C versus B on GFA and found that the small replacement (≤ 5 at %) of C by B increases the maximum attainable diameter up to 2.7 mm while further B addition leads to deterioration of t_{max}. In 2004 Fe–Cr–Mo–(Y, Ln)–C–B (Ln=Lanthanides) bulk amorphous steels with maximum diameter thickness of 1.2 cm were successfully fabricated by the injection casting technique [48]. Yittrium was selected as a candidate element due to the following reasons: 1) Y atoms have big sizes so they can help to suppress the nucleation and growth of

crystalline phases during cooling because they increase the packing density of the alloy liquid, 2) Y can decrease the content of oxygen in the melt by formation of Y-oxide leading to a high stability of the remaining melt. Replacement of Y by Dy in $Fe_{50}Cr_{14}Mo_{14}C_{14}B_6Y_2$ amorphous steel increased the T_{rg} but was not very effective on thermal stability of this alloy. Sheng et al [76] investigated the substitution of a portion of B by Sm in the $Fe_{43}Cr_{16}Mo_{16}C_{15}B_{10}$ alloy in order to further improve its GFA and mechanical behavior. Substitution of 1 at% B by Sm results in the widest supercooled liquid region (ΔT_x=88 K). When the Sm content is more than 1 at %, the thermal stability is dramatically reduced. They also observed a strong effect of Sm replacement for 1-4 at% B on the GFA so that the critical diameter for glass formation of the Sm modified alloy reached a value as large as 5 mm by copper mold casting. Gu et al. [21] reported the important effect of appropriate amount of Er on the GFA of Fe-Cr-Mo-C-B which could lead to produce rods with diameter of 12 mm.

4.1.3.2 Effect of Cr on GFA of $Fe_{65-x}Cr_xMo_{14}C_{15}B_6$

Most amorphous steels have alloying elements added to modify their properties and this can be used for specific applications. It is well known that adding Cr to amorphous steels tremendously increases the corrosion and oxidation resistance of this family of metallic glasses [42, 65]. On the other hand, as it has been mentioned, any change in the composition and constituent elements of a system could affect the GFA and thermal stability of amorphous phase. Therefore, it is necessary to study the influence of Cr addition on GFA and the thermal stability of this amorphous steel. Although

the Inoue's empirical rules give useful directions to choose an easy glass former system and composition, these are rather general, and the development of new amorphous alloys is guided by empirical rather than theoretical considerations.

In order to estimate the GFA of $Fe_{65}Mo_{14}C_{15}B_6$ amorphous steel and study the effect of replacing Fe by Cr, the thermal characterization study of the prepared ribbons was carried out by differential scanning calorimetry (DSC) at the heating rate of 20 K/min

The obtained values of the glass transition temperature (T_g), the first crystallization event (T_x), the solidus temperature (T_m) and liquidus temperature (T_l) are reported in Table III.

Table.III Values of the characteristic temperatures and GFA parameters of the $Fe_{65-x}Cr_xMo_{14}C_{15}B_6$ alloys.

Addition of Cr element	Tg	Tx	Tm	T_l	ΔT_x	T_{rg}	γ	γ_m	δ	ω	φ
x=0	515	550	1077	1145	35	0.555	0.373	0.605	1.306	0.243	0.378
x=2	519	562	1083	1150	43	0.556	0.376	0.617	1.323	0.233	0.389
x=4	526	576	1091	1160	50	0.557	0.380	0.627	1.339	0.225	0.398
x=6	531	579	1097	1163	48	0.560	0.381	0.626	1.348	0.226	0.397
x=8	532	580	1103	1170	48	0.558	0.379	0.624	1.336	0.227	0.395
x=10	536	581	1105	1183	45	0.556	0.377	0.617	1.319	0.232	0.391
		Ideal values			0.0	1.0	0.5	1.0	∞	0.0	0.0

Using these transformation temperatures, several parameters generally

employed to indicate the thermal stability and GFA of amorphous alloys, can be calculated: the super-cooled liquid range $\Delta T_x=T_x-T_g$, the reduced glass transition temperature $T_{rg}=T_g/T_l$, $\gamma=T_x/(T_g+T_l)$, $\gamma_m=2T_x-T_g/T_l$, $\delta=T_x/(T_l-T_g)$, $\omega=T_g/T_x-(2T_g/(T_g+T_l))$ and $\varphi=T_{rg}(\Delta T_x/T_g)^{0.143}$.

All these parameters are summarized in Table III. Ideal values for highest GFA are defined in the limit where T_g, and T_l are equal to each other [5]. The ΔT_x value for the alloys studied in this work is in the range from 35 to 48 K. The largest ΔT_x value was obtained for x=4 at.% alloy which reveals the highest thermal stability. It was found that T_{rg} was almost independent of the chromium content and kept at constant value of about 0.55 in the composition range between 0-10 at.% Cr for the present alloys. Although the calculated parameters for Cr content between 4 and 8 at.% are remarkably close to each other, it was found that the different criteria defining the highest GFA correspond to the alloys either with 4 or 6 at.% Cr. The alloy with 6 at.% of Cr has the highest values of γ and δ. On the other hand, according to the values of γ_m, ω and φ the alloy with 4 at.% of Cr has the best glass-forming ability. This fact can be explained because the super-cooled liquid region is considered in these last three GFA criteria.

The radius of Fe and Cr atoms are very close to each other and the mixing enthalpy of Fe-Mo and Cr-Mo binary systems are almost the same. So according to the mixing enthalpy of binary Fe-C and Fe-B atomic pairs which are more positive than that of Cr-C and Cr-B, the replacement of Fe by Cr is expected to increase the thermal stability and GFA of Fe-Cr-metalloid glassy alloys. But it is also very important for a system to be at or

near its eutectic composition for easy glass formation. According to the melting behavior, no single melting peak is observed in the DSC measurements (Fig. 4.4) of these six alloys indicating that they are not at eutectic points. The shortest melting interval (T_l-T_m) corresponds to the alloy with 6 at.% of Cr being therefore the closest alloy to the eutectic point. By combining these results, it can be said from the present study that considering γ and δ criteria, the best glass forming alloy is the one closest to a eutectic composition. It can be also noticed that the alloy with 10 at.% of Cr has the largest melting interval while does not have the poorest GFA among these six alloys.

4.2 Devitrification

Microstructural analysis was carried out on isothermally annealed Cr4 ribbons at different temperatures up to 800°C (for 20 min) using XRD, SEM and HRTEM in bright field (BF) and selected area electron diffraction (SAED) modes.

4.2.1 XRD

Figure 4.6 presents the XRD patterns of the Cr4 alloy in the as-quenched and heat treated states. The annealing temperatures of 400°C, 500°C, 580°C, 600°C, 650°C and 800°C were selected to completely cover the structural relaxation-crystallization temperature range obtained by DSC.

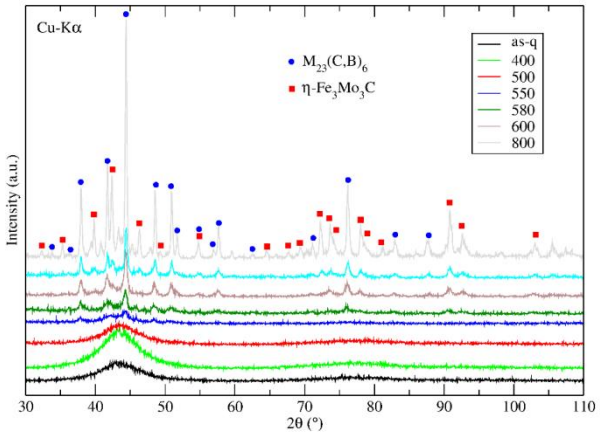

Figure 4.6 XRD patterns of Cr4-alloy obtained after heat treatments at different annealing temperatures.

The alloys do not show any obvious crystallization even after annealing at 500°C, as evidenced by the diffuse peaks at around 2Θ~45° in the XRD profile of these alloys. However, the amorphous hump becomes somewhat narrower and higher with respect to that of the as-quenched sample which indicates some structural changes corresponding to the structural relaxation. The significant changes are noticed for the samples annealed at or above 580°C (after the initial crystallization has occurred), where peaks corresponding to crystalline phases appear. These peaks have been identified as $M_{23}(C, B)_6$ (with M=Fe,Mo) solution produced in amorphous matrix. The absence of sharp peaks in the XRD profiles of low temperature annealed samples means that the amorphous phase is thermally stable up to approximately 550°C. With increasing annealing temperature, the peaks

become narrower and the intensity of the diffraction peak increases, suggesting that the crystallinity of the annealed samples increases and the crystalline grains size increases which will be confirmed later by TEM and SEM examinations.

When the temperature is increased to 650°C (above the secondary crystallization temperature), another crystalline phase is observed. The new formed diffraction peaks were identified to be the η-Fe_3Mo_3C crystalline phase and like the former crystalline phase become narrower and more intense at higher temperatures. Fully crystallization can be observed in the alloys isothermally annealed at 800°C composed by the η-Fe_3Mo_3C and $M_{23}(C, B)_6$ phases as the two final crystallization products.

According to DSC and structural analysis, it can be concluded that the first and second crystallization peaks on the DSC trace shown in Fig. 4.4 are associated with $M_{23}(C, B)_6$ and η-Fe_3Mo_3C phases precipitations respectively.

4.2.2 SEM

Figure 4.7 displays SEM micrographs of Cr4 ribbons as a function of annealing temperatures. The amorphous nature is clearly evident in the SEM image of the as-quenched sample and the samples annealed at 400°C and 500°C. The white spots observed in the sample annealed at 500°C are probably related to dust or external particles.

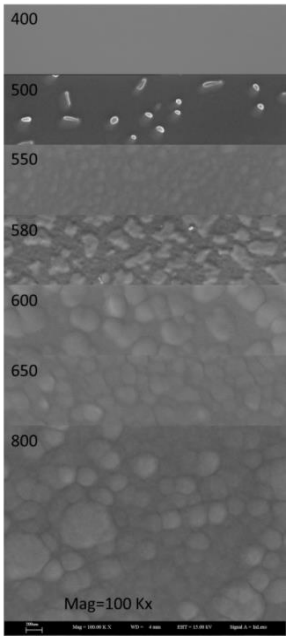

Figure 4.7 SEM micrographs of the surface of Cr4 alloy heat treated at different temperatures.

A fine microstructure and uniform distribution of particles can be seen in the samples annealed at 550°C-800°C. In the samples annealed at 550°C and 580°C, a substantial fraction of crystallized particles embedded in the amorphous matrix is observed but the glassy phase still dominates the microstructure in these alloys which is compatible with the XRD result. From the visual observations, as the temperature increases the glassy phase fraction is reduced because of increasing either the number density or the size of the particles dispersed in the amorphous matrix. The number density of the particles increases evidently in the sample annealed at 650°C where the second crystalline phase starts forming. At the final stages of

crystallization at higher temperatures only the average size of the particles increases and the number density and the uniform distribution of the crystals stays constant. The significant size growth is observed when the temperature was increased to 800°C where the crystalline grains exceed 100 nm.

4.2.3 TEM

In order to achieve a more precise microstructure analysis, the microstructural evolution of the Cr4 annealed at 550°C, 580°C, 600°C and 800°C was studied by HR-TEM. Figure 4.8 shows the TEM bright-field images of the alloys with inserted corresponding SAD patterns.

The samples annealed at 550°C and 580°C show a dense and uniform distribution of fine crystalline grains. The grain size of the crystalline phase was typically in the range 10 – 20 nm. The mixture of an halo ring and some diffraction spots from $M_{23}(C, B)_6$ phase in the SAD patterns indicate the presence of the remaining amorphous phase with some embedded crystals in these heat treated alloys. By increasing the temperature, the intensity of the halo ring becomes weaker suggesting that the glassy phase is disappearing.

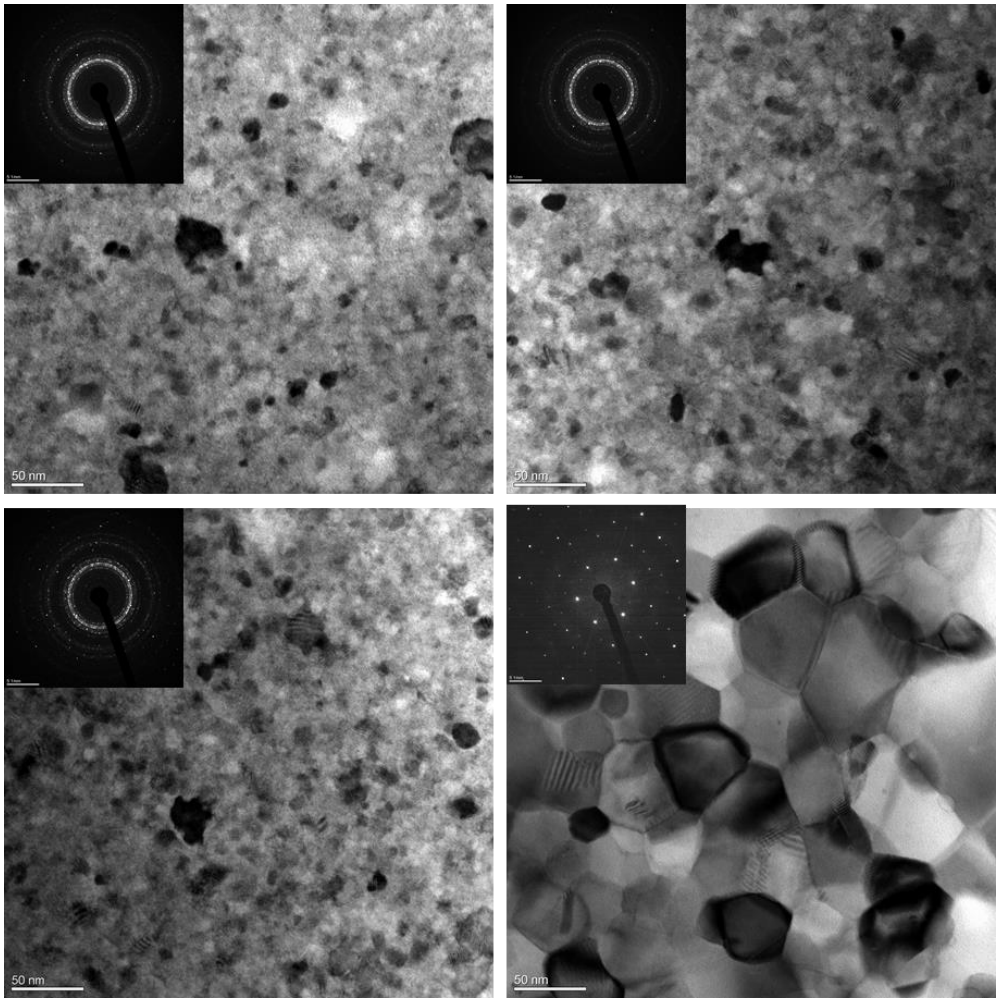

Figure 4.8 TEM images of Cr4-alloy annealed at 550 ºC (left-top) 580ºC (right-top), 600 ºC (left-bottom) and 800ºC (right-bottom).

HR-TEM images of the samples annealed at 550°C and 580°C are shown in Figs. 4.9 (A) and (B), respectively.

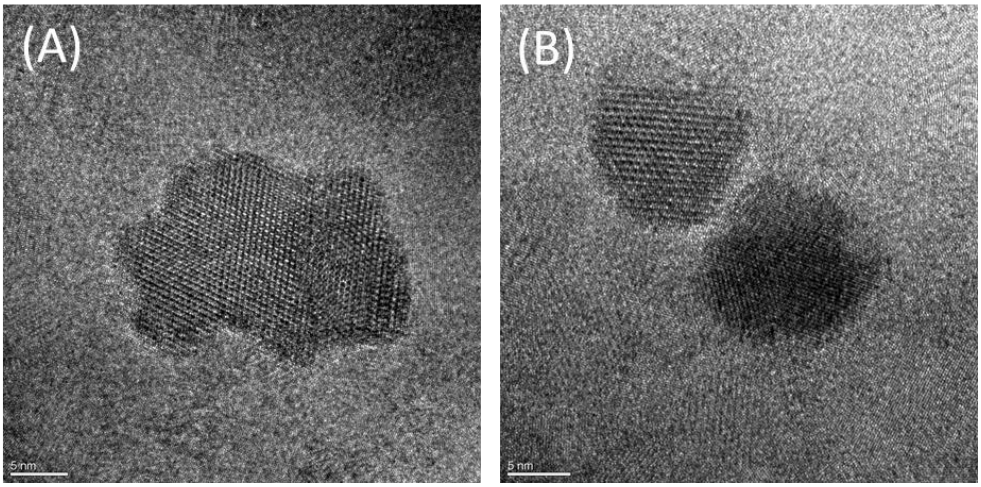

Figure 4.9 HRTEM image of Cr4-alloy heat treated at 550 ^{o}C (A) and 580 ^{o}C (B) showing $M_{23}(C,B)_{26}$ nanocrystals embedded in the amorphous matrix.

In the center of the images we can see crystal grains but it can be seen that a substantial amount of glassy phase still remain in both samples with different fractions. Observations from several parts showed that the amorphous phase exists around most of the particles of these two states. These surrounding particle free zones are less extended in the sample annealed at 580°C, indicating that the fraction of the glassy phase becomes smaller by the heat-treatment temperature. BF-TEM micrograph of the sample annealed at 600°C reveals an extremely high number density of nanocrystals with the average size of 15nm embedded in the amorphous matrix. The electron diffraction pattern of the selected area taken from this alloy contains weak halo rings, indicating that the matrix of the crystalline phases is still amorphous.

BF-TEM image of the Cr4 subjected to an isothermal treatment at 800°C for 20 min shows a fully crystallized structure with an average grain size of 50 nm. No residual amorphous phase can be detected in this alloy and the amorphous matrix is fully devitrified at this temperature. This also is confirmed with the corresponding SAD pattern which shows the presence of sharp diffraction spots indicating the formation of well-developed crystalline phases. In order to identify the final produced phases of this alloy, Nano-beam electron diffraction (NBD) and EELS element mapping have been performed in this specimen annealed at 800°C. Figure 4.10 shows a compositional map of the final microstructure obtained for the Cr4 alloy.

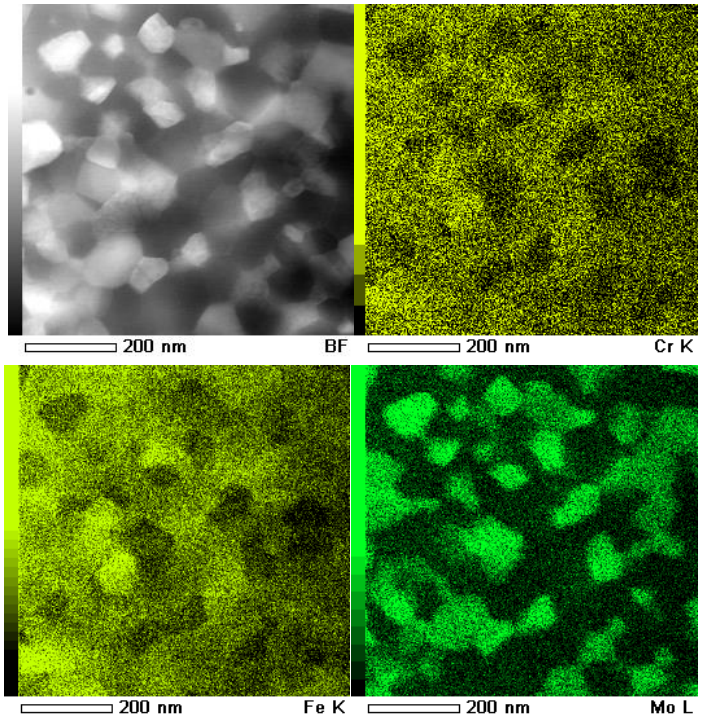

Figure 4.10 Compositional map of Cr4-alloy heat treated at 800° C.

Brighter contrast depicts higher concentration of the element at the location. This compositional map shows the Fe, Cr and Mo distribution in the fully crystalline state. The different crystalline grains observed in the Bright Field image can be clearly identified with Mo-rich and (Fe,Cr)-rich zones, respectively. As shown in figure 4.11, the NBD analysis of these regions proves that Fe-rich and Mo-rich grains corresponds to $(Fe,Cr)_{23}(C,B)_6$ and η-Fe_3Mo_3C phases respectively.

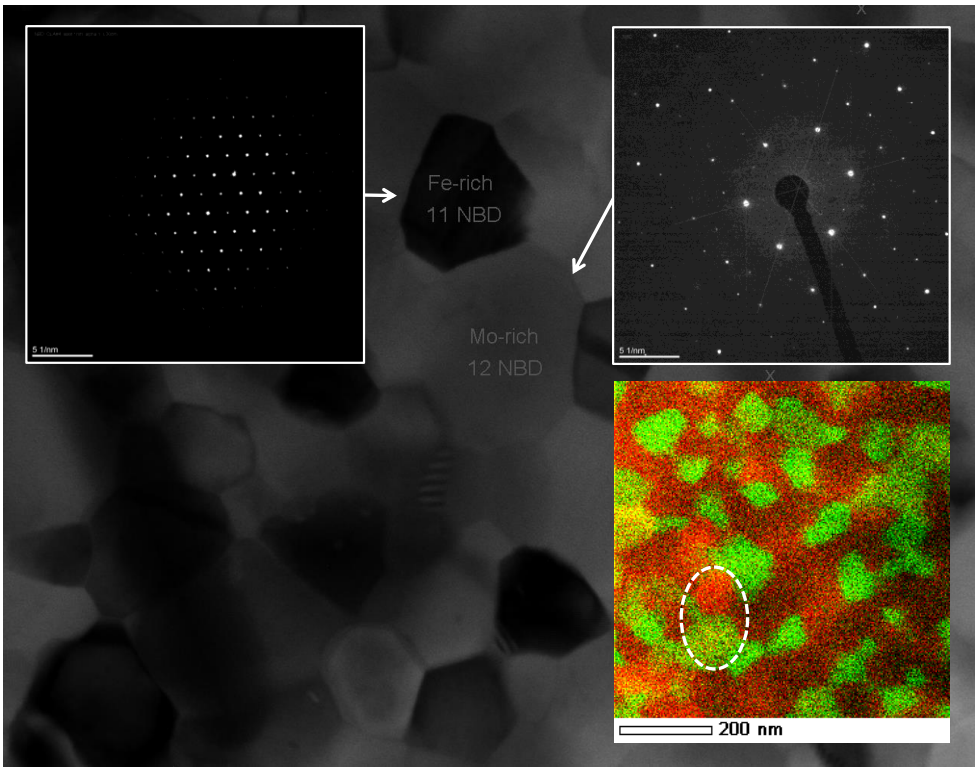

Figure 4.11 NBD analysis of the final microstructure obtained after heat treatment of Cr4-alloy at 800 ºC showing that Fe-rich and Mo-rich zones correspond to $M_{23}(C,B)_6$ and M_6C phases respectively. The compositional map (right-bottom) shows the Fe-Cr rich (red) and the Mo-rich (green) grains, the dashed line indicates the analyzed area.

The presence of these phases is consistent with the crystalline phases obtained from XRD for the alloy in this annealing condition. As it is mentioned before, one of the aims of this work is to replace Fe by a suitable amount of Cr in order to obtain desired properties, such as mechanical and corrosion resistance, so it is crucial to know whether the constituent phases and devitrification path depend on the composition or not. Comparing the

Synchroton XRD patterns of Cr0 annealed at 800°C (Figure 4.12) and devitrified Cr4 demonstrates that the final crystalline phases in the sample without Cr are the same found in the sample with low Cr content.

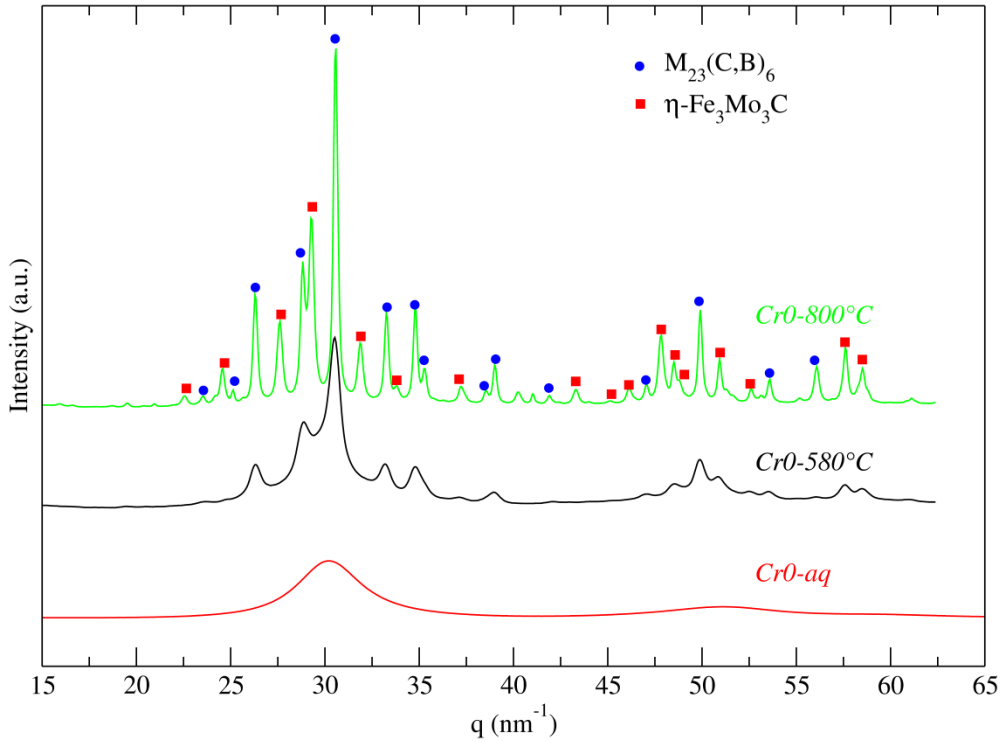

Figure 4.12 Synchrotron XRD patterns of Cr0-alloy as-produced, heat treated at 580 °C and heat treated at 800 °C.

Also the same phases ($M_{23}(C,B)_6$ and η-Fe_3Mo_3C) are identified as the main crystallization products for high Cr-content alloy (Cr15) as described in detail by Duarte et al. [77, 78]. This reveals that the terminal structure of all the series, Cr0-Cr15 is not significantly dependent on the Cr content

although the metastable phases formed during devitrification are not necessarily the same.

4.3 Corrosion

4.3.1 Effect of Cr on Corrosion of $Fe_{65-x}Cr_xMo_{14}C_{15}B_6$

In order to evaluate the corrosion behavior, the amorphous ribbons were exposed to immersion and polarization environments. Immersion experiments were performed in glass bottles containing 100ml of 6 N H_2SO_4 solution at 295 K open to air. After 168 hours, the specimens were removed from the test solution, washed in distilled water and dried. The weight reductions of each specimen after immersion were measured. Immersion tests were repeated 3 times for each specimen. Corrosion rates can be determined by the weight-loss method, which can be calculated from the following equation [79]:

$$Corrosion\ rate(mm/year) = \frac{87.6 \times W}{A \times T \times D} \qquad 4.1$$

here W is the total weight loss in milligram after exposure, A is the exposure area of the specimen in cm^2, T is the exposure time in hours, and D is the density of the alloy in g/cm3.

Figure 4.13 shows the respective corrosion rates of all the ribbons in this aggressive solution.

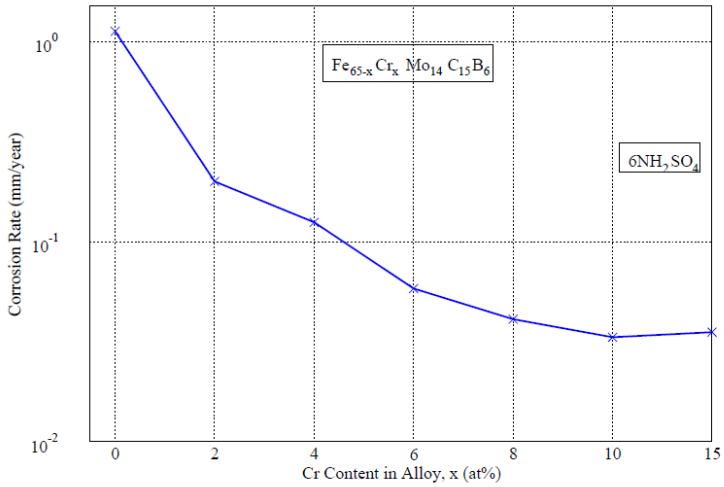

Figure 4.13 Corrosion rates of the $Fe_{(65-x)}Cr_xMo_{14}C_{15}B_6$ amorphous alloys in 6 N H_2SO_4 plotted versus chromium contents.

The glassy ribbons containing 2 at.% and 4 at.% of Cr had already low corrosion rates of ~10^{-1} mm/year in 6 N H_2SO_4 solution at room temperature, this is one order of magnitude lower than the Cr free alloy. For alloys containing 6 or more at.% of Cr the corrosion rate dropped substantially. Increasing the Cr content further does not produces drastic changes in the dissolution rate obtaining values in the range between 2×10^{-2} and 5×10^{-2} mm/year. For comparison, the high Cr alloy with x = 15 at.% [78], has been also tested showing a corrosion rate of the same order of magnitude than those obtained for x = 6.

In addition to the immersion tests, faster potential sweep measurements have been performed to gain additional information on the initial potential-dependent corrosion behavior. Figure 4.14 shows a typical potentiostatic polarization response of the Cr4 alloy in 0.1 N H_2SO_4 at the applied potential of +1 V vs. Ag/AgCl. The current density firstly dropped rapidly at the very first stage of polarization and then stabilized and remains stable at low current density, confirming that all the testing samples were in a stable state.

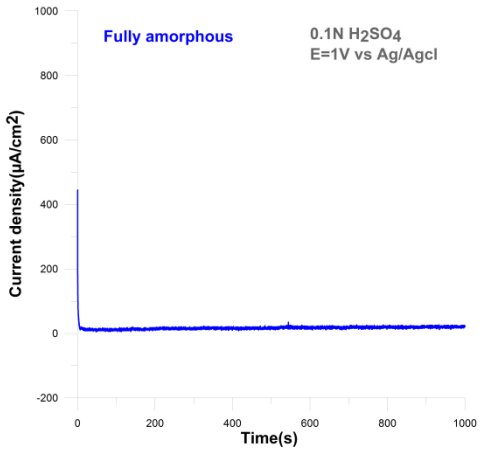

Figure 4.14 Current density as function of time for Cr4 amorphous alloy at +1 V in 0.1 N H_2SO_4 open to air.

The electrochemical measurements in 0.1 N H_2SO_4 solution, shown in Figure 4.15, indicate that the samples without and with 2 at.% of Cr show a rather active-like behavior in H_2SO_4 compared to samples containing higher amounts of Cr. The respective steep rise in current corresponds to the known transpassive Mo dissolution observed for Mo-based alloys. For more than 6 at.% Cr the samples exhibit similar polarization behavior to each other and are spontaneously passivated with a relatively wide passivation region and

low passive current densities. In addition, it is also seen that the alloys containing a larger amount of chromium show lower passive current densities (see inset) but almost the same breakdown potential. Such a dependence of the passive current on the Cr content was earlier reported by Kirchheim for crystalline Fe–Cr alloys [80].

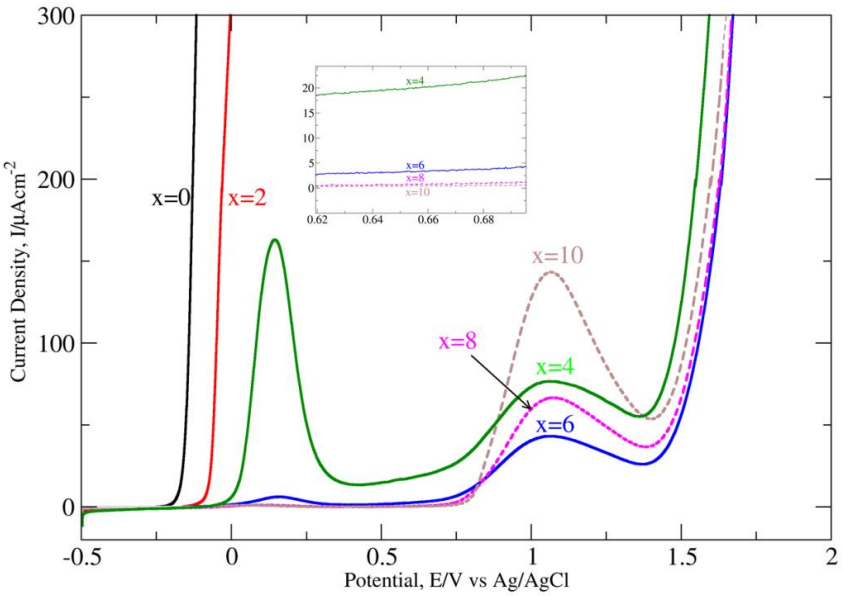

Figure 4.15 Linear polarization sweeps for $Fe_{65-x}Cr_xMo_{14}C_{15}B_6$ (x=0, 2, 4, 6, 8 and 10 at. %) in 0.1 N H_2SO_4 solution obtained at 2 mV/s.

The sample containing 4 at.% Cr shows a very pronounced transition peak at about 0.2 V which indicates the transformation of an existing native oxide layer (with an oxide reflecting the bulk composition) towards a Cr-rich passive film. The passive current observed during the potential sweep is for

this sample also considerably higher than for the samples with even higher Cr content. For all alloys containing 4 at.% of Cr and more, a current plateau or a further peak is visible which extends from about 0.8 V up to a steep rise in current at about 1.5 V vs. Ag/AgCl. This strong electrochemical current at about 1.5 V has its onset approximately at the usually observed transpassive Cr dissolution of pure Cr, while Fe-based alloys are typically shifted to lower values (showing a co-dissolution effect). While the potentiodynamic scans are thus instructive for the formation of the initial passive film at lower potentials, a more exact description of the breakdown behavior requires at this point more information of the specific surface states or on gas evolution reactions, which might be also involved but cannot be distinguished from current measurements alone. This is, at this point, beyond the scope of the presented initial screening experiments and will be addressed in future work. From the results obtained for 0.1 N H_2SO_4 it can be said that more than 4 at. % of Cr should be included in the Fe–Cr–Mo–C–B system to form a passive film leading to a reasonably high corrosion resistance. Figure 4.16 shows SEM micrographs of the surface of x = 0, 4 and 8 alloys after the polarization tests in 0.1 N H_2SO_4 for 1000 s at the breakdown potential.

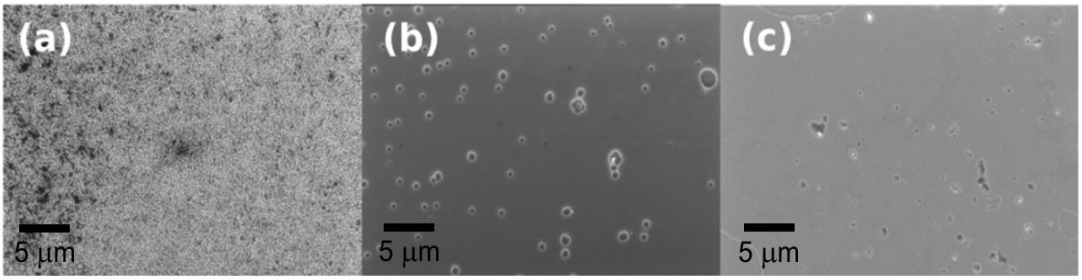

Figure 4.16 SEM micrographs of the surface of polarized $Fe_{65}Mo_{14}C_{15}B_6$ (a), $Fe_{61}Cr_4Mo_{14}C_{15}B_6$ (b) and $Fe_{57}Cr_8Mo_{14}C_{15}B_6$ (c) ribbons for 1000s in 0.1N H_2SO_4 at break-down potentials.

These images show that as Cr increases in the composition, the corroded surfaces are less damaged. In Fig. 4.16a) the surface of the alloy with x = 0 is completely damaged related to an increase of the corrosion products. In Fig. 4.16(b) several round-shaped micrometer-sized pits-like regions are visible for the alloy with *x*=4 whereas in Fig. 4.16(c) still some pores or pits are observed on the surface with *x*=8. However, its surface is less damaged in comparison to the sample without Cr and 4 at.% of Cr. Moreover, the pores observed in the alloy with 8 at.% resemble to selective dissolution of Cr-depleted regions probably dependent of inhomogeneities in the composition on the surface [78,81]. It is known that Cr is one of the most effective alloying elements providing a high passivating ability for the Fe–Cr–metalloid glassy alloys [69, 82]. Corrosion resistance in metallic glasses is enhanced by producing spontaneous passivation related to the formation of a thin homogeneous film of Cr oxide. In general, compared to stainless steels which require a minimum 13 at.% Cr, this glassy alloy system needs only 4–

6 at.% of Cr for achieving stable passivity. Nevertheless a pitting-type of attack is visible for these alloys close to break-down potentials.

The rate and extend of corrosion depend not only on structural and compositional features, but also on the various environmental conditions. The environmental determining factors include: pH value, concentration, temperature, pressure, fluid flow of electrolyte, availability of oxygen, mechanical stress, time of exposure to a corrosive medium and presence of biological organisms. Exposure to different corrosive media with different characteristic and nature, leads to formation of different corrosion products and since the corrosion rate of metals and alloys is controlled by the formation of a passive film, the comparison between different solutions in correlation with the corrosion behavior of the material is very important.

The corrosion mechanism of some Fe-based metallic glasses changed in different corrosive mediums. Recent studies on the electrochemical behavior of Fe-based metallic glasses in acidic and neutral solutions have shown that these materials are more susceptible to corrosion in acidic media [83].

The passivation of the metallic glasses was shown to be sensitive to the concentration of H^+ ions while the breakdown mechanism is mostly governed by Cl^- ions. Also several investigations were hold about the effect of the concentration and the temperature of the test environment on corrosion behavior of Fe-based metallic glasses [75, 84]. Pang et al. [42] investigated the effect of concentration on the corrosion rate of $Fe_{56}Cr_{16}Mo_{16}C_{18}B_4$ BMG. The corrosion rate for the sample examined in 12 M HCl was one order of magnitude greater than the one tested in 1 M HCl. This alloy was spontaneously passivated in aggressive 6 M HCl solution with wide passive

region, low passive current and no pits were observed on the surface. Higher general and localized attack in more concentrated solutions is expected but it is important to find the maximum concentration at which the alloy or the corrosion products are electrochemically immune.

In Figure 4.17, the potentiodynamic curves at room temperature for all the samples in the HCl solution are shown in semi logarithmic axis. Samples x=0 and x=2 does not show any passive region and spontaneously corrode at very low values of the potential. For x=4 and x=6, the curves are similar with a relatively small active-passive region followed by a large passive region with a double step characteristic of these Fe-based compositions [85]. But the alloy with higher Cr content presents a transpassive metal dissolution and/or oxygen evolution at higher values of the potential.

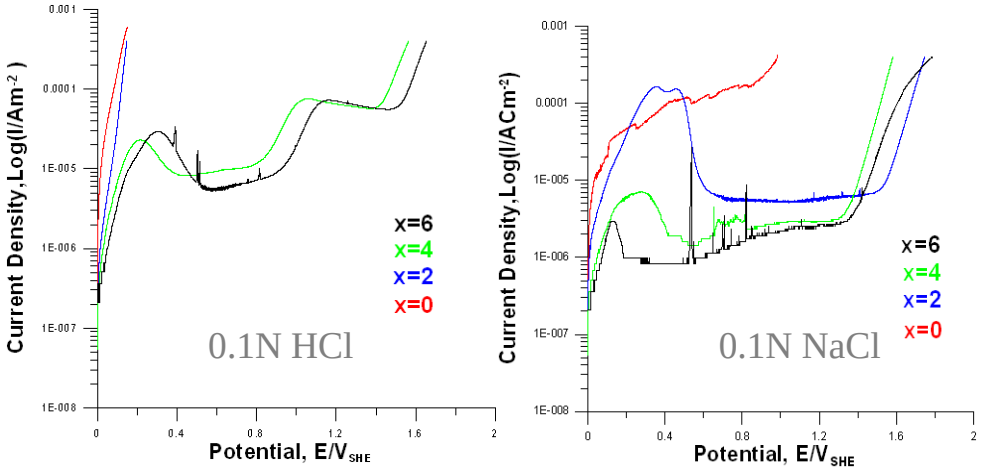

Figure 4.17 Linear polarization sweeps for $Fe_{65-x}Cr_xMo_{14}C_{15}B_6$ (x=0, 2, 4, and 6 at. %) in 0.1 N HCl (left) and 0.1N NaCl (right) solution obtained at 2 mV/s.

This better corrosion resistance for the *x*=6 sample is also demonstrated by the lower passive current density in the first passive region. The values of the breakdown potential and the passive current density for all the samples and the two used solutions can be found in Table IV.

Table IV The Values of breakdown potential and passive current density in 0.1 N HCl and 0.1 N NaCl

Electrolyte	HCl				NaCl			
Cr content (at.%)	0	2	4	6	0	2	4	6
E_b (V)	-	-	1.3	1.5	-	1.45	1.3	1.35
ln I_P (A/m^2)	-	-	$1x10^{-5}$	$8x10^{-6}$	-	$7x10^{-6}$	$4x10^{-6}$	$2x10^{-6}$

For the NaCl solution, Figure 4.17 (right) shows that the Cr free alloy has a very low corrosion resistance and no passivation at all, similarly to what happen in the HCl solution. For *x*=4 and *x*=6, we also find a similar behaviour with a small active-passive region, more important in the case *x*=4, and a large passive region, longer and with a lower passive current density for *x*=4. The most important difference between the two solutions appears at *x*=2 where in the NaCl solution a passive film is created yielding a wide passive region. Moreover, the breakdown potential for *x*=2 is higher than for *x*=4 and *x*=6, showing that in NaCl solutions the best alloy in terms of corrosion resistance is not the one with highest Cr content, as is the case for the HCl solutions.

Chromium is one of most effective elements to improve the corrosion and oxidation resistance of amorphous and conventional crystalline alloys. But the difference is in the amount of Cr needed which is much higher in the crystalline alloys [86]. Chromium is a reactive metal which has high affinity for oxygen [87]. The oxide film formed on the Cr surface acts as a barrier that isolates it from the majority of environments [88]. According to XPS studies, Cr tends to be concentrated in the passive film during exposure to corrosive media due to the tendency to oxidation [89, 90]. Chromium oxide is very unreactive and is more thermodynamically stable than the oxides of iron. Chromium has the electron configuration $<Ar>3d^5 4s^1$, i.e. 6 electrons outside the argon configuration. This element is protected in oxidizing conditions by the formation of continuous inert oxides, which acts as a barrier between the metal and the environment [91]. As a transition metal, Cr has a broad range of oxidation states (from - 2 to + 6), but only the + 3 and + 6 states are stable under most conditions of the surface environment. Other forms of oxides will tend to be converted to trivalent and +6 oxides which are very slow to react at concentrations ranging from tenths to even hundreds of mg/l [92].

Naka et al. [64] reported the enhanced corrosion resistance of amorphous Fe-C alloy by adding Cr and/or Mo. An XPS analysis applied before and after immersion test of Cr-containing alloy has shown that the passive film formed on the amorphous alloy in acidic solutions containing chloride ions consisted exclusively of hydrated chromium oxyhydroxide ($CrO_x[OH]_{3-2x}.nH_2O$). Since Cr-enriched passive film is found to be responsible for the high corrosion resistance, most of the investigations have been done on Fe-based metallic glasses with high amounts of Cr.

The role of Cr in increasing the corrosion resistant of Fe-based amorphous alloys is discussed in a number of papers by Hashimoto [93], Pang [65], Asami [70] and Wang [94]. Pang et al. Investigated the polarization behavior and immersion test of $Fe_{60-x}Cr_xMo_{15}C_{15}B_{10}$ (x=0, 7.5, 15, 22.5 and 30 at.%) glassy alloy. This alloy showed high corrosion resistance in 1N HCl solution [42]. Increase of Chromium content improved the corrosion resistance of this glassy alloy. The same group reported the beneficial effect of adding P or partial replacement of: 1) Mo with Nb and Ta or 2) Fe with B on the corrosion resistance of this family of Fe-based metallic glasses [40, 42].

Asami et al. studied the influence of molybdenum on polarization behavior of a high Cr content (25 at.%) of Fe-Cr-Mo-B amorphous alloy in 6N HCl. Although formation of passive film facilitated by adding 5% of molybdenum, this element did not form its own passive film and lowered the corrosion potential and increased the passive current density [95]. Some amorphous Fe-Cr-Mo-metalloid alloys passivate spontaneously even in hot 12 N HCl [66]. The protective film becomes more stable and pitting corrosion resistance increases when the inner Mo-oxide film formed is covered by chromium-enriched layer but the pitting inhibition efficiency of Mo-oxide is strongly influenced by the Cr/Mo ratio. For example detrimental effect of Mo on corrosion resistance was reported in high Mo content (22.5 at. %) Fe-Cr-Mo-C-B glassy alloy [66] so it is very important to choose an optimal Cr/Mo ratio.

1.4.1. Effect of heat treatment on corrosion behavior

In order to understand the influence of the structural changes on the corrosion behavior, polarization measurements were performed on as-quenched, relaxed and crystallized samples. Here we selected the Cr4 alloy as a representative of the studied alloys. The Cr4-alloy is the composition with lowest content of Cr showing a passivation reaction and a trans-passive region in all the studied solutions. The specimens were heat treated at 400°C, 500°C, 580°C, 600°C, 650°C and 800°C, following the procedure described in section 3.3. Polarization measurements were performed in 0.1N H_2SO_4 at room temperature.

The current vs. time curves at constant potential of as-quenched and fully crystalline Cr4 in 0.1 N H_2SO_4 at the applied potential of +1 V vs. Ag/AgCl are shown in figure 4.18. The current density of the fully amorphous Cr4 dropped rapidly at the very first stage of polarization and then stabilized and remains stable at low current density. This implies that no corrosion initiated on the alloy surface exposed to solution or in the initial stage of the passive film formation the corrosion minimized and this protective film stays compact until the last stages of exposure. In contrast, the current densities of the fully crystalline sample increased during the first few seconds of exposure but then decreased with time. The current densities after 15 minutes exposure for crystalline sample (132 μAcm^{-2}) was one order of magnitude higher than that of amorphous sample (11 μAcm^{-2}) at the same test condition. This can be attributed to the formation of a porous passive film with a large amount of defects on this sample as will be confirmed later by visual observations. In the later stages of the passive film formation (i.e. the

time is above 400 s), the compactability of the passive film tends to be decreased and it becomes more porous.

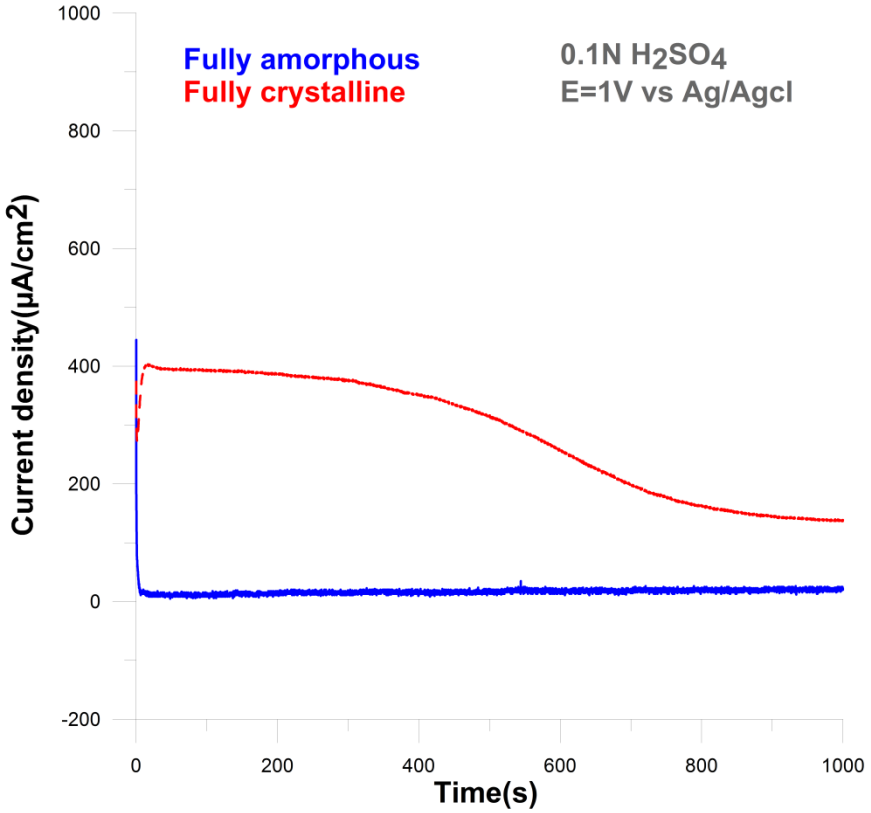

Figure 4.18Current density as function of time for Cr4 amorphous and crystlalline samples at +1 V in 0.1 N H_2SO_4 open to air.

The potentiodynamic polarization curves of the as-quenched and heat treated samples are shown in Figures 4.19 and 4.20.

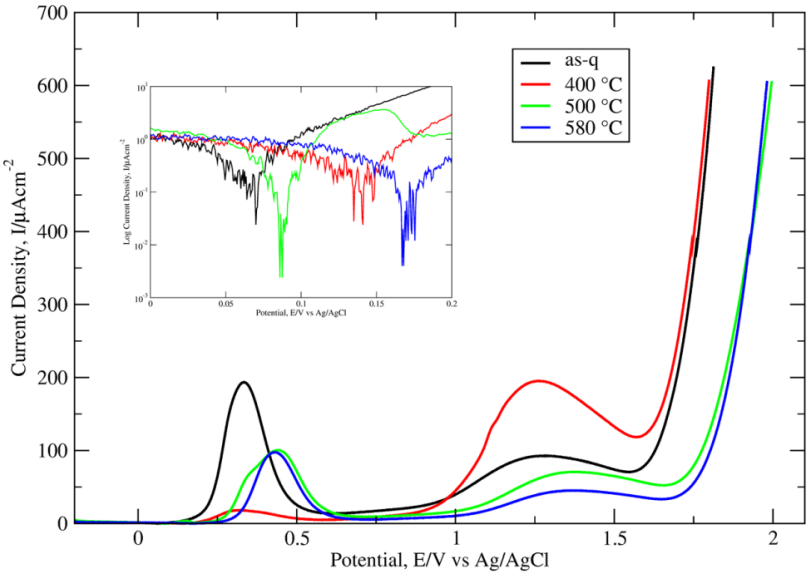

Figure 4.19 Potentiodynamic curves of the Cr4-alloy as produced and after heat treatments up to 580 ^{o}C.

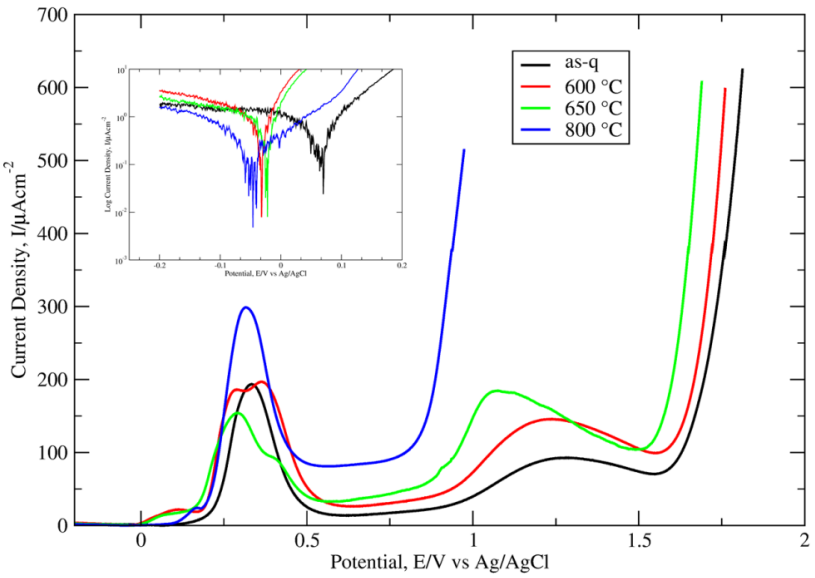

Figure 4.20 Potentiodynamic curves of the Cr4-alloy as produced and after heat treatments above 600 ^{o}C.

It is clear that untreated and annealed samples exhibit similar polarization behavior with almost similar Tafel slopes in different regions. The anodic parts of the potentiodynamic scans show an increase in current densities for small values of the anodic potential. Subsequently, an active-to-passive transition and current passivation area are detected with the corresponding decrease and plateau in the current density. When the anodic voltage becomes larger, the current density for all the annealing temperatures except 800 ºC, presents a second peak possibly due to a re-passivation phenomena.

According to the anodic part of the potentiodynamic scans, for heat treatments below 580 ºC the breakdown potential (E_b) increases while the passive current density (I_{pass}) decreases (with a transition behavior for the sample heated at the lowest temperature). For the samples annealed above 580 ºC the opposite behavior is observed, i.e. a decrease in E_b and an increase in I_{pass}. These two parameters, together with the corrosion potential (E_{corr}), the corrosion current density (I_{corr}), the critical passive current density (I_{crit}) and the passive region (E_b - E_{corr}) can be obtained from Figures 4.19 and 4.20 and are shown in Table V. Also the correlation between these parameters and the different structural states, i.e. amorphous, relaxed, partially and fully crystallized, of the alloys determined by XRD and TEM are shown.

Table. V Electrochemical parameters obtained from potentiodynamic polarization curves

Heat treatment (°C)	E_{corr} (V vs Ag/Agcl)	I_{corr} ($\mu A/cm^2$)	I_{crit} ($\mu A/cm^2$)	I_{pass} ($\mu A/cm^2$)	E_b-E_{corr} (V)	Structure
As produced	0.06	0.7	194	57	1.47	Amorphous
400	0.16	0.63	18	55	1.48	Relaxed
500	0.11	0.61	100	37	1.51	Relaxed
580	0.19	0.54	97	24	1.52	Amorphous + $M_{23}(C,B)_6$
600	-0.03	0.83	197	61	1.44	Amorphous + $M_{23}(C,B)_6$ + M_6C
650	-0.02	0.85	154	72	1.40	Amorphous+ $M_{23}(C,B)_6$ + M_6C
800	-0.04	0.9	299	97	0.83	Fully crystallized

Figure 4.21 summarizes the evolution of the corrosion parameters as function of the applied heat treatment. The sample annealed at 800°C exhibits the lowest corrosion potential (E_{corr}=-0.03 V), as expected because it corresponds to the fully crystalline sample.

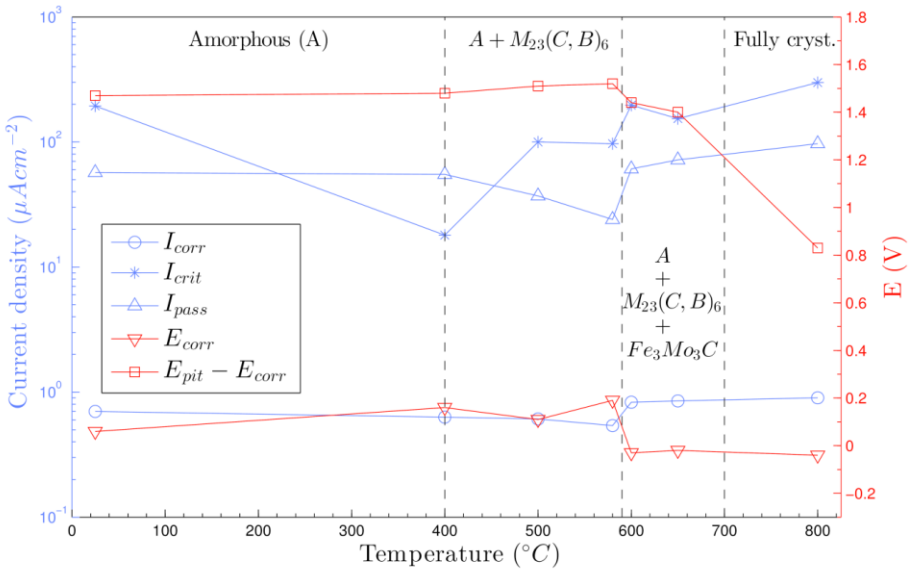

Figure 4.21 Summary of the corrosion parameters obtained for the Cr4-alloy after different annealing protocols.

This parameter increases for annealing temperatures up to 580°C. It is interesting to note that E_{corr} is almost constant for annealing treatments at temperatures higher than 600°C, i.e., after the second crystalline phase appears. On the contrary, the corrosion current density, I_{corr}, smoothly diminishes as the annealing temperature increases until the η-Fe_3Mo_3C phase appears (around 600 ºC); afterwards it increases and reaches values higher than the initial ones. The passivation range (E_b - E_{corr}) is maximized (1.52 V) for the sample annealed at 580 ºC, showing the same tendency than the corrosion potential, i.e., an increase up to 600 ºC and a subsequent decrease, especially important for the fully crystallized sample.

Therefore, the more pitting resistant sample is the one with nanocrystalline $(Fe,Cr)_{23}(C,B)_6$ phase embedded in an amorphous matrix. The critical passive current density, I_{crit}, is an indication of the passivating capability of the material: the lowest I_{crit} the highest the easiness of creating a passive layer. Thus, all the samples annealed below 600 ºC have a tendency to create a passive layer, being the relaxed completely amorphous sample the one with the best passivation capacity. Finally, the passive current density, I_{pass}, presents the same behavior as I_{corr}, decreasing until the second crystalline phase appears and increasing afterwards being maximum for the completely crystallized sample. The decrease in I_{pass} by annealing shows that a more protective passive film forms after relaxation and partial nano-crystallization. Summarizing, these results show that among all the samples, the partially crystallized one (with $(Fe,Cr)_{23}(C,B)_6$ nanocrystals embedded in an amorphous matrix) possesses the best corrosion behavior, i.e., the highest E_{corr}, the widest passive region E_b - E_{corr}, and the lowest I_{corr} and I_{pass}.

The corrosion morphology was investigated using the SEM. The SEM photographs of polarized ribbons are shown in Figures 4.22 and 4.23. In Figure 4.22 it is seen that the number and size of pits increase with the temperature of the annealing pre-treatment. For the samples annealed up to 580°C (Fig. 4.22c) there is no visible pit and they do not suffer from any pitting or film breaking. These observations confirm that the samples annealed at temperatures that allow the crystallization of the η-Fe_3Mo_3C phase, the corrosion damage becomes more serious.

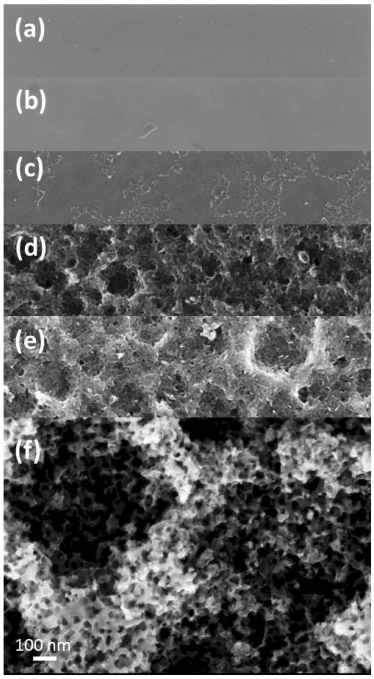

Figure 4.22 SEM micrographs of the surface of polarized Cr4 ribbons for 1000s in 0.1N H_2SO_4 at break-down potentials after annealing at (a) 400 ºC, (b) 500 ºC, (c) 580 ºC, (d) 600 ºC, (e) 650 ºC and (f) 800 ºC.

Figure 4.23 shows SEM images of the surface and cross-section of wide and shallow pit-shaped cavities propagation in fully crystallized Cr4 sample. It can be seen that not all the surface is attacked entirely. Some zones in the surface remain almost un-attacked as they form a more protective layer, presumably of high concentrated CrOOH [66]. The pit initiation sites are possibly the Cr-depleted areas which favor the protective film break down. The thick corrosion product layer can be attributed to the pseudo-passive

film growth during constant potential exposure experiment which was performed after the anodic polarization measurements.

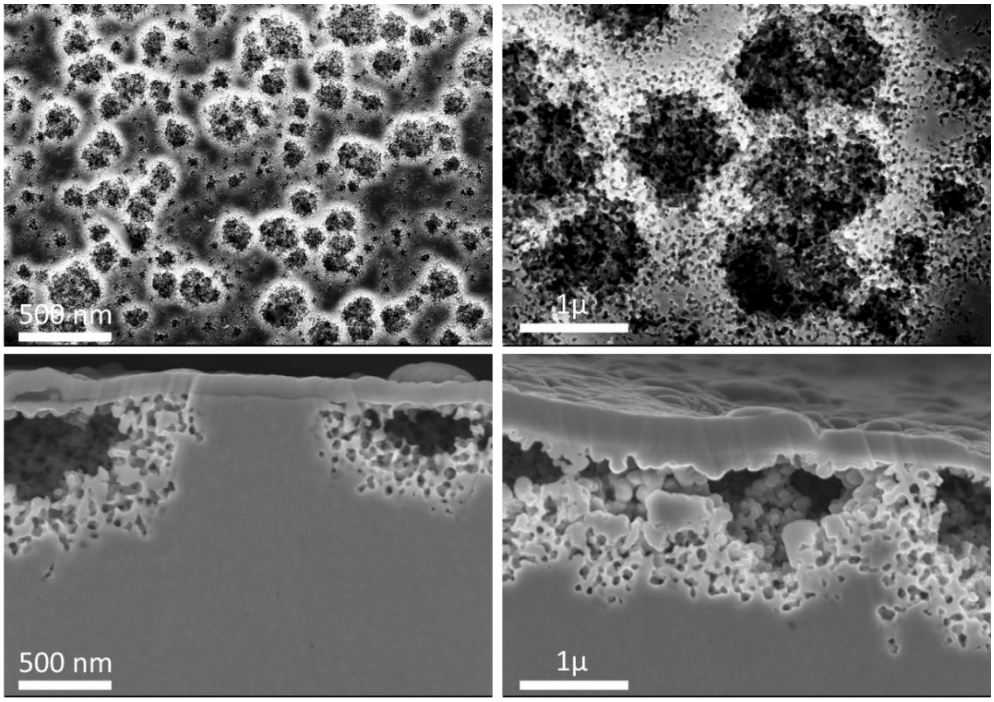

Figure 4.23 SEM images of the surface and cross-section of pit-shaped cavities propagation in fully crystallized Cr4 sample polarized for 1000s in 0.1N H_2SO_4 at break-down potentials.

As it is mentioned in section 4.1.2, alloys in melt-spun states contain a significant amount of free volume. The free volume as a structural feature can affect the corrosion resistance of the amorphous alloys. Since the structural relaxation causes atomic rearrangement, free volume decreases (by forming a denser amorphous structure) and leads to the improvement of corrosion resistance. The structural relaxation releases the quenched-in

stresses of the glass leading to an increase in chemical stability by decreasing the dissolution activity of alloying elements in the amorphous structure.

Better corrosion resistance in structurally relaxed than in as-produced amorphous counterparts was obtained in Fe-Cr-P-C-Si [96], Fe-B-Si [97], Fe-Ni-P-B [98], (Fe-Co)-B-Si-Nb [67] alloys but not observed in Fe-Cr-W-P-C [99] and Fe-Cu-Nb-Si-B alloys [100].

Although XRD (Figure 4.6) and TEM (Figure 4.8) results revealed that heat treatment of the Cr4 sample annealed at 580°C led to a dispersion of nano-scale $(Fe,Cr)_{23}(C,B)_6$ crystallites in an amorphous matrix, its corrosion resistance is higher compared to the fully amorphous and relaxed samples annealed at 400°C and 500°C. The mechanism of such improvement is still unknown but it seems that the negative effect on the corrosion resistance of the galvanic coupling between the $(Fe,Cr)_{23}(C,B)_6$ phase and the residual amorphous matrix is negligible. Moreover, the defects caused by these ultra-fine grains seem not to affect the homogeneity and protective properties of the passive layer. Two possible explanations for the higher corrosion resistance of this nano-crystalline/amorphous composite can be as following: 1) nanocrystalline materials contain a large amount of grain boundaries and interfacial volume which promote the diffusion of, mainly, Cr but also other passive-film-formation elements like Mo. This may induce a faster formation of the passive layer leading to more protectiveness [101]. 2) As the higher annealing temperature results in greater structural relaxation and a reduction of free volume, the remaining amorphous matrix has a more homogeneous structure.

Further heat treatment changes the structure to a two phase mixture with Cr-rich and Mo-rich grains. Although the samples annealed at 600°C and 650°C have some remaining amorphous areas, the formation of the new crystalline phase (η-Fe_3Mo_3C) leads to a deterioration of the corrosion resistance when compared with the samples untreated or annealed up to 580°C. Similar behavior was reported by Yang et al. [102], Souza et al. [103], Belkhaouda et al. [96], Bakara et al. [104] and Pardo et al. [105] for some other Fe-based metallic glasses. The samples annealed at 800°C showed even more deterioration in the corrosion resistance. The heat treatment to this temperature leads to the fully crystallization of the sample and the enlargement of the crystalline grain sizes to about 50 nm. As the grains grow, crystalline defects increase and more grain boundaries are formed which are favorable for corrosion initiation. In this fully crystallized samples the galvanic coupling between $(Fe,Cr)_{23}(C,B)_6$ and η-Fe_3Mo_3C leads first to the dissolution of the Cr-depleted zones.

It is known that in Cr-containing Fe-based alloys, Mo prevents the dissolution of Cr by rapid formation of a protective molybdenum oxide film in the potential regions where Cr actively dissolves [93]. Also Molybdenum oxide films formed in active regions cause a lower passive current density and higher localized (pitting and crevice) corrosion resistance when covered by a chromium-enriched oxyhydroxide layer [83, 93, 101 and 106].

The very short passivation range with a distinct current density (almost one order of magnitude greater than other samples) is observed in the fully crystallized alloy. When the Mo-rich grains exceed the critical limit of 50nm, Cr-rich passive film cannot cover them completely and, therefore, the Mo-

oxide film is not effective on corrosion resistance in passive region any more. The exact mechanism of the passive layer in the studied compositions is currently under investigation and will be published elsewhere.

4.4 Mechanical Properties

4.4.1 Mechanical behavior of Fe-based amorphous alloys

Lacking the dislocations and crystalline lattice, metallic glasses show unusual deformation behavior. These materials exhibit strength much closer to the theoretical strength of the material but negligible plasticity at low temperature [107, 108]. Although precipitation of a second phase or addition of reinforcement particles to the amorphous matrix has been shown to increase the plasticity of some metallic glasses, these composite approaches limits their use in scope of applications where a fully amorphous structure is required [17].

Fe-based metallic glasses in general, and in particularly amorphous steels are characterized by very high strengths and tendency to brittle fracture. Most Amorphous steels are reported to possess high strength over 3.5GPa but their plastic strain is usually less than 0.5% [109]. The plasticity of some amorphous steels is enhanced by partial substitution of Fe by small amounts of elements possessing high Poisson ratio (ν) values, but these replacements mostly change the deformation and fracture response, and leads to strength degradation. In situ formation of nano-scale phases in amorphous matrix composites has a double-edged effect on the deformation behavior in relation to monolithic Fe-based metallic glasses. Mechanical response of in situ composites is strongly affected by the nature of the crystalline phase and the crystallized volume fraction. Dispersion of ductile α-Fe dendrites in the amorphous matrix promotes the generation of multiple shear bands, thus

improving the plasticity, while formation of brittle $Fe_{23}B_6$ deteriorates the plasticity [110, 111].

The Fe-Mo-C-B family has fracture strengths going from 3.5 to 4.4 GPa but some compositions show ability to sustain a little amount of compressive plastic strain (below 1%) at room temperature [109]. Although small, this plastic strain is among the largest in Fe-based metallic glasses. The addition of Cr to the quaternary base composition increases the elastic constants. The Poisson ratio decreases from ν=0.334 ($Fe_{65}Mo_{14}C_{15}B_6$) to ν=0.322 ($Fe_{59}Cr_{15}Mo_{14}C_{15}B_6$) and fracture changes from ductile to fragile behavior. Plastic strain at room temperature is not observed for Cr contents >10 at%. The Poisson ratios of these series are in the range of critical values of ν corresponding to the brittle-to-tough transition in the case of Fe-based metallic glasses [112, 113]. For these reason it is interesting to examine the effect of small changes in Cr addition on the mechanical response.

4.4.2 Effect of Cr on mechanical behavior

The mechanical properties of Fe-Cr-Mo-C-B amorphous ribbons were evaluated using the technique of nano-indentation. This technique is a proper technique due to the low ductility of Fe-based metallic glasses. Furthermore, the surface mechanical behavior of these alloys is substantial as they are expected to be applied as corrosion and wear resistant protective covers. During a typical nanoindentation test, force and penetration are recorded as the load is applied to the indenter with a prescribed loading and unloading profile. The smaller the penetration depth the harder is the material.

Figure 4.24 shows the variation of indentation load as a function of indenter penetration depth into the cross-section of representative as-quenched ribbon samples, obtained in a loading rate of 0.25mN/s. The maximum load (P_{max}) used is 50 mN.

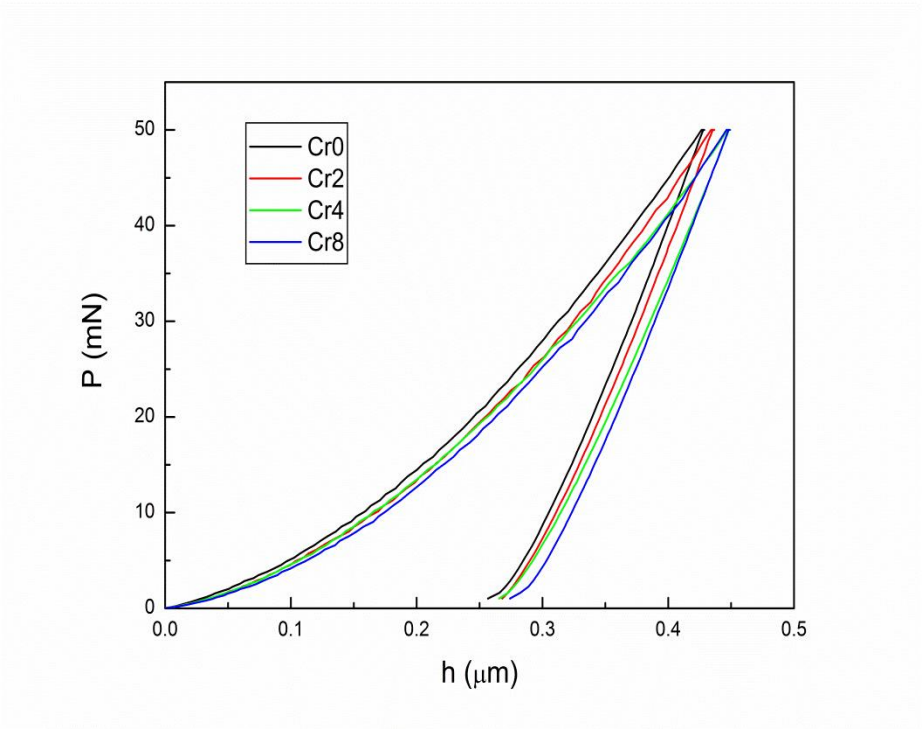

Figure 4.24 Load-depth diagram.

The unloading segments of the *load–depth* response illustrate inelastic (elastoplastic) deformations. The inhomogeneous plastic deformation of glassy alloys occurs by propagation of *shear bands* [114]. Shear formation in metallic glasses which have been attributed to the local decrease in the viscosity of the glass, results in a sudden drop in the load [5, 115]. Shear banding in amorphous metals can be considered one example of a

mechanical instability. The loading portions of the curves do not present discontinuous plastic flow referred to as shear banding events. The absence of shear band activity is somewhat in agreement with the SEM observations. Figure 4.25 shows the typical indent on the Cr-free and the Cr6 samples.

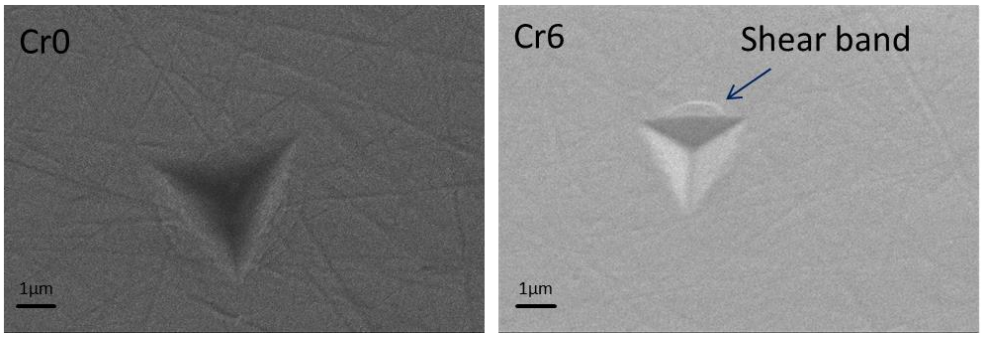

Figure 4.25 SEM images of the indent on Cr0 (left) and Cr6 (right) amorphous ribbons.

In agreement with the results obtained in some metallic glasses, cracks and shear bands are rather scarce in these samples although one circular shear band marking is visible on the one side of the indentation impression in Cr6 sample.

The Oliver and Pharr method [116] was used for analyzing the data to obtain hardness and elastic modulus. The hardness is expressed as a ratio of peak load (P_{max}) to the contact area (A_c) as given below:

$$H = \frac{P_{max}}{A_c} \qquad 4.2$$

Where the contact area (A_c) is a function of contact depth (h_c): $A_c = f(h_c^2)$ and the contact depth (h_c) is defined as the function of maximum displacement of

the tip (*i:e*. penetration depth at $P_{\max}$) and unloading stiffness ($S = \frac{dP}{dh}|_{h=h_{max}}$) at maximum load:

$$h_c = h_{max} - \epsilon \frac{P_{max}}{S}; \quad 4.3$$

The elastic modulus of the sample (E) is determined by the following equation:

$$S = \beta \frac{2}{\sqrt{\pi}} E_r \sqrt{A} \quad 4.4$$

Where β is the King's factor, that depends on the geometry of the indenter (β = 1.034 for a Berkovich indenter). E_{r} is the reduced Young's modulus defined as follow:

$$\frac{1}{E_r} = \frac{1 - v^2}{E} + \frac{1 - v_i^2}{E_i} \quad 4.5$$

E_{r} is then the effective modulus of the combined system of indenter and sample. Where v and v_i are the Poisson's ratio of the sample and indenter

respectively, E_i is the elastic modulus of the indenter material (for diamond indentor, E_i = 1140 GPa and ν_i = 0.07).

Table VI lists the hardness (H) and reduced elastic Modulus (E_r) of the as-quenched ribbons. In order to obtain more information about the trend of mechanical properties by Cr addition, we also measured the mentioned parameters for Cr15 as representative of high Cr content alloys.

Table VI The measured values of nanoindentation test for $Fe_{65-x}Cr_xMo_{14}C_{15}B_6$ (x=0, 2, 4, 6, 8, 10 and 15 at. %) glassy ribbons.

Addition of Cr element	$H(GPa)$	E_r (GPa)	H/E_r	U_e (nJ)	U_p (nJ)	U_{tot} (nJ)	U_e/U_{tot}
Cr0	15.61 ± 0.12	179.4 ± 1.8	0.0870	3.783 ± 0.028	4.483 ± 0.056	8.266	0.457
Cr2	15.61 ± 0.08	175.8 ± 0.9	0.0888	3.882 ± 0.022	4.388 ± 0.025	8.270	0.469
Cr4	15.50 ± 0.13	166.7 ± 0.8	0.0929	4.082 ± 0.014	4.379 ± 0.022	8.461	0.482
Cr6	15.64 ± 0.15	156.6 ± 2.0	0.0999	4.336 ± 0.044	4.343 ± 0.035	8.679	0.499
Cr8	15.29 ± 0.06	170.6 ± 0.9	0.0896	3.993 ± 0.025	4.396 ± 0.015	8.389	0.475
Cr10	15.23 ± 0.08	173 ± 0.8	0.0888	3.910 ± 0.08	4.109 ± 0.012	8.519	0.488
Cr15	16.60 ± 0.07	184.1 ± 0.6	0.0902	3.801 ± 0.023	3.932 ± 0.01	7.730	0.508

As seen in Table.VI the hardness of $Fe_{65-x}Cr_xMo_{14}C_{15}B_6$ (x=0, 2, 4, 6, 8, 10 and 15 at. %) amorphous ribbons exhibit no compositional dependence. This very high hardness (H > 15 GPa), is in agreement with other Fe-based metallic glasses [117]. The Young's modulus E_r varies from 179 Gpa of Cr0 to 184 GPa of Cr15. Increasing Cr content up to 6 at.%, resulted in decreasing the Young's modulus E_r but further increasing Cr content caused an increase in E_r. The ratio of hardness to elastic modulus H/E_r, gives

an indirect assessment of the wear resistance [118, 119]. A material with higher H/E_r ratio elastically recovers the deformation induced by external stress. The experimental results (listed in table VI) reveal that H/E_r ratio for these alloys is ~0.09 and somewhat increases with increasing the Cr content. These high values of H/E_r ratio indicate that all the samples have excellent wear resistance.

The area below the loading curve corresponds to the energy for the total indentation deformation U_{total}. The values of $U_{elastic}$ were calculated from the area between unloading curve and the displacement axis. The difference of U_{total} and $U_{elastic}$ gives the plastic deformation energy:

$$U_{plastic} = U_{total} - U_{elastic} \qquad 4.6$$

The elastic recovery (μ) was evaluated as the ratio between the elastic and the total (plastic+elastic) energies during nanoindentation, $U_{elastic}/U_{total}$.

Table.VI also lists the $U_{elastic}$, U_{total} and μ values of Cr(0-15) alloys. The μ value is increased from 0.457 to 0.508 with increasing Cr content from 0 to 15 at.%. The highest μ value is achieved for Cr15 which has the highest hardness. The higher hardness provides a sample with a higher resistance to local plastic deformation so that the U_{total} decreases.

In conclusion, all measured values do not differ significantly between the investigated materials with Cr contents <10 at%. The highest hardness value corresponds to the sample containing 15 at%. of Cr. Concerning wear

properties, the best wear resistance is obtained for Cr6 and the highest elastic recovery is also achieved for Cr15. However, the changes observed for the different alloys are small and the effect of the particular relaxation state achieved during the ultrarapid solidification may determine more significantly the mechanical behavior than the alloy composition. The effects of structural relaxation and nano-crystallization on mechanical behavior are worth to be studied in the future.

5 Conclusions

Iron-based metallic glasses, with the nominal composition of $Fe_{65-x}Cr_xMo_{14}C_{15}B_6$ (x=0, 2, 4, 6, 8 and 10 at. %), as the typical representation of Fe-Mo-C-B system, were selected for investigation in this study. A detailed study on the effect of low amount of Cr on the Glass forming ability, corrosion resistance and mechanical behavior has been done in order to determine the optimal amount of Cr needed to obtain good corrosion and mechanical properties while maintaining a high GFA. Also thermally induced structural transformations (structure relaxation and crystallization) behavior and their effect on the corrosion resistance were investigated.

The composition showed drastically different effects on the different properties of the alloy depending on the amount of Cr. The temperature interval of the super-cooled liquid region (ΔT_x) values were found in the range from 35 to 48 K and, in particular, partial replacement of 4 at.% Fe by Cr revealed the widest ΔT_x, therefore the highest thermal stability. It was found that the change in reduced glass transition temperature (T_{rg}) with Cr content is negligible. According to the assessment of other GFA criteria (γ, γ_m, δ, ω and φ), the alloys containing 4 and 6 at.% were found to be the best glass formers in this system although a high GFA is expected in all the series. According to the melting intervals, the alloy with 6 at.% of Cr was the closest one to an eutectic composition.

In order to evaluate the corrosion behavior, the amorphous ribbons were exposed to electrolytes with different pH values. The alloys containing more

than 4 at.% of Cr were spontaneously passivated with low current densities in dilute H_2SO_4 and HCl whereas the alloys with Cr content <4 at.% showed dissolution above the Mo transpassive potential. From the anodic polarization curves of the passive alloys, only a slight improvement (more noble values) of the breakdown potential and passive current density were obtained for higher Cr-contents in the range between 6 and 10 at.%. Corrosion rates measured by immersion tests in aggressive acid logically decreased with an increase of chromium content in the alloys. The obtained values showed high corrosion resistance for all the compositions from x = 6 to 10 at.%. The substitution of 4–6 at.% Fe by Cr is then enough for enhancing the corrosion resistance for this Fe-based amorphous system in acidic media although pitting like behavior was observed. In neutral solution, Cr-free alloy exhibited an active behavior but only a 2% addition of Cr resulted in a sufficiently high corrosion resistance which was demonstrated by a wide passive region.

Increasing the Cr content did not produce any trend in mechanical properties, unlike the other properties. The hardness values did not differ significantly between the materials with different amounts of Cr and Young's modulus was found to be more sensitive to the Cr-content. Wear properties revealed that all the samples have excellent wear resistance. The highest plastic recovery was achieved for the Cr-free alloy and increasing Cr content clearly deteriorated the plasticity.

The crystallization processes observed by DSC were similar in all compositions but regularly shifted to higher temperatures by the addition of Cr. The phase evolution upon heating of these amorphous alloys proceeded

by two crystallization reactions: upon annealing around T_{x1}, uniform distribution of crystallites of $M_{23}(C,B)_6$ phase of 10-20 nm in size embedded in amorphous matrix were detected, but the glassy phase was still dominant. Upon Annealing up to T_{x2}, the glassy phase fraction was reduced because of the increase of the number density and the size of the particles dispersed in the amorphous matrix. Finally, on annealing beyond T_{x2}, significant crystallization was observed which was composed by the η-Fe_3Mo_3C and $M_{23}(C, B)_6$ as the two final crystallization products.

Electrochemical measurements of the heat treated samples unveiled a strong dependence of corrosion resistance on structural transformation. Annealed samples exhibited similar polarization behavior as the as-produced samples, with almost similar Tafel slopes in different regions. Although structural relaxation improved the corrosion resistance by forming a more ideal glass, the best corrosion resistance was obtained for the sample showing a structure consisting of nanocrystalline Cr-rich phase embedded in an amorphous matrix (i.e., after annealing at intermediate temperatures between T_{x1} and T_{x2}). Precipitation of a second crystalline phase (Mo-rich) had a detrimental effect on corrosion resistance but the alloys exhibited good anticorrosion properties until the Mo-rich grains exceed the critical limit of 50 nm, where the Cr-rich passive film was not able to cover them completely. For high Cr-content alloys, selective dissolution of the Mo-rich phase as a new strategy for synthesis of mesoporous materials was reported [78]. This Fe,Cr-rich carbide mesoporous structure also appeared in low Cr compositions. This characteristic is expected to be useful for applications in corrosive

environments where a high specific surface area is required like catalysts or battery electrodes.

These results show that Fe–Cr–Mo–C–B alloys with remarkable GFA, high thermal stability, high hardness, as well as superior corrosion and wear resistance can be obtained with Cr additions near 5 at.%. Corrosion and wear often combine to cause aggressive damage in a number of industries. The combination of good corrosion and wear resistance, make these materials good candidates for applications with mechanical/environmental interactions.

Higher Cr-content (Cr>6 at.%) alloys are better candidates only for applications where plasticity is not an issue and the material is exposed to aggressive environments. Although alloys with relatively low Cr contents exhibited the best plasticity among all the studied alloys, their high tendency to corrode limits their applications to inert environments.

Finally, we hope this work will be useful for guiding the selection of new alloys for a specific application or working environment. The results presented here aims to give guidance on how to select the composition and post synthesizing annealing protocol for achieving the best compromise between corrosion-resistance, thermal stability and surface mechanical properties.

6 References

[1] Luborsky, F. E. (ed.) Amorphous Metallic Alloys (*Butterworths, London, 1983*)

[2] Wang, W.H., C. Dong, and C.H. Shek. Bulk metallic glasses. *Mater. Sci. Eng. Rep*. R 44: 45–89. (2004)

[3] Elliott, S. R. "Physics of amorphous materials." (1983)

[4] Klement, W., R.H. Willens, and P. Duwez. Non-crystalline structure in solidified gold–silicon alloys. *Nature* 187: 869–870. (1960)

[5] C. Suryanarayana, A. Inoue, Bulk Metallic Glasses, (*Taylor & Francis, US, 2011*).

[6] D. Turnbull, M.H. Cohen, *Journal of Chemical Physics*, 31, 1164 (1961)

[7] Kui, H.W., A.L. Greer, and D. Turnbull. Formation of bulk metallic glass by fluxing. *Appl. Phys. Lett*. 45: 615–616. (1984)

[8] Johnson, W.L. Thermodynamic and kinetic aspects of the crystal to glass transformation in metallic materials. *Prog. Mater. Sci*. 30: 81–134. (1986)

[9] A. Inoue, T. Nakamura, N. Nishiyama, T. Masumoto, Mater. Trans. JIM 33 937. (1992)

[10] M. Telford. The case for bulk metallic glass. *Materialstoday*, 7 36-43. (2004)

[11] H. M. Chen, Y. C. Chang, T. H. Hung, X. H. Du, J. C. Huang, J. S. Jang, P. K. Liaw, *Materials Transactions*, Vol 48, No. 7 pp. 1802-1805. (2007)

[12] Miller, Michael K., and Peter Liaw. Bulk metallic glasses: an overview. *Springer Science & Business Media,* (2007)

[13] C. Suryanarayana, A. Inoue, *International Material Reviews*, Vol. 58, No.3, 131. (2013)

[14] J. Fornell, S. González, E. Rossinyol, S. Suriñach, M. D. Baro, D. V. Louzguine-Luzgin, J. H. Perepezko, J. Sort, A. Inoue, *Acta Materialia* 58 6256-6266. (2010)

[15] Jorg F. Loffler, *Intermetallica* 11 529-540. (2003)

[16] A. Makino, A. Inoue, T. Masumoto, *Materials Transacions*, JIM, Vol. 36, No. 7 pp. 924-938. (1995)

[17] M. M. Trexler, N. N. Thadhani, *Progress in Materials Science* 55 759-839. (2010)

[18] J. Shen, Q. J. Chen, J. F. Sun, H. B. Fan and G. Wang: 'Exceptionally high glass-forming ability of an FeCoCrMoCBY alloy', *Appl. Phys. Lett*., 86, 151907-1–151907-3. (2005)

[19] A. Inoue, A. Takeuchi, *Acta Mater*. 59 2243e2267. (2011)

[20] A. Inoue, Y. Shinohara, J. S. Gook, *Materials transactions*, JIM, Vol. 36, No. 12, pp. 1427-1433. (1995)

[21] X. J. Gu, S. Josep Poon, *Journal of Materials Research*, Vol. 22, No. 2, (2007)

[22] Turnbull, D. Under what conditions can a glass be formed? *Contemp. Phys*. 10: 473–488. (1969)

[23] Z.P. Lu, Y. Li, S.C. Ng, *Journal of Non-Crystalline Solids* 270 103-114. (2000)

[24] Nielsen, H.J.V. The eutectic compositions as a basis for the formation of metallic glasses in the binary alloys of iron-group transition metals with metalloids. *Z. Metall*. 70: 180–184. (1979)

[25] Wang, W.H., J. Lewandowski, and A.L. Greer. Understanding the glassforming ability of Cu50Zr50 alloys in terms of a metastable eutectic. *J. Mater. Res*. 20: 2307–2313. (2005)

[26] Inoue, A. Stabilization of metallic supercooled liquid and bulk amorphous alloys. *Acta Mater*. 48: 297–306. (2000)

[27] Inoue, A. Stabilization of metallic supercooled liquid and bulk amorphous alloys. *Acta Mater*. 48: 279–306. (2000)

[28] Donald, I.W. and H.A. Davies. Prediction of glass-forming ability for metallic systems. *J. Non Cryst. Solids* 30: 77–85. (1978)

[29] Hruby, A. Evaluation of glass-forming tendency by means of DTA. *Czech. J. Phys. B* 22: 1187–1193. (1972)

[30] Lu, Z.P. and C.T. Liu. A new glass-forming ability criterion for bulk metallic glasses. *Acta Mater*. 50: 3501–3512. (2002)

[31] Du, X.H., J.C. Huang, C.T. Liu, and Z.P. Lu. New criterion of glass forming ability for bulk metallic glasses. *J. Appl. Phys*. 101: 086108-1–086108-3. (2007)

[32] Mondal, K. and B.S. Murty. On the parameters to assess the glass forming ability of liquids. *J. Non-Cryst. Solids* 351: 1366–1371. (2005)

[33] Chen, Q.J., J. Shen, D. Zhang, H.B. Fan, J.F. Sun, and D.G. McCartney. A new criterion for evaluating the glass-forming ability of bulk metallic glasses. *Mater. Sci. Eng. A* 433: 155–160. (2006)

[34] Long, Z.L., H.Q. Wei, Y.H. Ding, P. Zhang, G.Q. Xie, and A. Inoue. A new criterion for predicting the glass-forming ability of bulk metallic glasses. *J. Alloys Compd*. 475: 207–219. (2009)

[35] Fan, G.J., H. Choo, and P.K. Liaw. A new criterion for the glass-forming ability of liquids. *J. Non-Cryst. Solids* 353: 102–107. (2007)

[36] J. Mao, H.F. Zhang, H.M. Fu, A.M. Wang, H. Li, Z.Q. Hu, *Adv. Eng. Mater*. 12 170. (2010)

[37] D. V. Louzguine-Luzgin, D.B Miracle, A. Inoue, *Adv. Eng. Mater*. 10 1008. (2008)

[38] Can glass stability parameters infer glass forming ability? Marcio L.F. Nascimento, Luciana A. Souza, Eduardo B. Ferreira, Edgar D. Zanotto. *Journal of Non-Crystalline Solids* 351 3296–3308. (2005)

[39] J. H. Yao, H. Yang, J. Zhang, J. Q. Wang and Y. Li: 'The influence of Nb and Zr on glass-formation ability in the ternary Fe–Nb–B and Fe–Zr–B and quaternary Fe–(Nb,Zr)–B alloy systems', *J. Mater. Res*., 23, 392–401. (2008)

[40] S. J. Pang, T. Zhang, K. Asami and A. Inoue: 'New Fe–Cr–Mo– (Nb, Ta)–C–B glassy alloys with high glass-forming ability and good corrosion resistance', *Mater. Trans*., 42, 376–379. (2001)

[41] Y. Hu, M. X. Pan, L. Liu, Y. H. Zhao, D. Q. Zhao, W. H. Wang. Synthesis of Fe-based bulk metallic glasses with low purity materials by multi-metalloids addition. *Materials Letters* 57. 2698 – 2701. (2003)

[42] S. J. Pang, T. Zhang, K. Asami and A. Inoue: 'Bulk glassy Fe–Cr– Mo–C–B alloys with high corrosion resistance', *Corros. Sci*., 44, 1847–1856. (2002)

[43] A. J. KAILATH, A. KUMAR and A. MITRA. Effect of metalloids on crystallization and magnetic behaviour of FeCoSiB based metallic glass. Bull. *Mater. Sci*., Vol. 29, No. 2, pp. 127–131. (2006)

[44] B. Zheng, Y. Zhou, J. E. Smugeresky, E. J. Lavernia. Processing and Behavior of Fe-Based Metallic Glass Components via Laser-Engineered Net Shaping, *Metallurgical and Materials Transactions A*, 1235-1245. (2009)

[45] Akira Takeuchi and Akihisa Inoue. Classification of Bulk Metallic Glasses by Atomic Size Difference, Heat of Mixing and Period of Constituent Elements and Its Application to Characterization of the Main

Alloying Element. *Materials Transactions*, Vol. 46, No. 12 pp. 2817 to 2829. (2005)

[46] O.N. Senkov, D.B. Miracle. Effect of the atomic size distribution on glass forming ability of amorphous metallic alloys. *Materials Research Bulletin* 36 2183–2198. (2001)

[47] K. Amiya and A. Inoue: 'Fe–(Cr, Mo)–(C, B)–Tm bulk metallic glasses with high strength and high glass-forming ability', *Rev. Adv. Mater Sci*., 18, 27–29. (2008)

[48] V. Ponnambalam, S. J. Poon and G. J. Shiflet: 'Fe-based bulk metallic glasses with diameter thickness larger than one centimeter', *J. Mater. Res*., 19, 1320–1323. (2004)

[49] Z. P. Lu, C. T. Liu, J. R. Thompson and W. D. Porter: 'Structural amorphous steels', *Phys. Rev. Lett*., 92, 245503-1–245503-4. (2004)

[50] H. E. Townsend. Effects of Alloying Elements on the Corrosion of Steel in Industrial Atmospheres. *Corrosion Science* Vol. 57, No. 6, pp. 497-501. (2011)

[51] P. Peled, S. Harush, D. Itzhak. The effect of Ni addition on the corrosion behaviour of sintered stainless steel in H_2SO_4. *Corrosion Science* Volume 28, Issue 4, Pages 327‑329. (1988)

[52] A. J. Sedriks. Effects of Alloy Composition and Microstructure on the Passivity of Stainless Steels. *Corrosion*, Vol. 42, No. 7, pp. 376-389. (1986)

[53] A. Nasery Isfahanya, H. Saghafiana, G. Borhani. The effect of heat treatment on mechanical properties and corrosion behavior of AISI420 martensitic stainless steel. *Journal of Alloys and Compounds* 509 3931–3936. (2011)

[54] J. L. Albarrana, L. Martinez, H. F. Lopez. Effect of heat treatment on the stress corrosion resistance of a microalloyed pipeline steel. *Corrosion Science* 41 1037-1049. (1999)

[55] P.P. Sarkar, P. Kumar, Manas Kumar Manna, P.C. Chakraborti. Microstructural influence on the electrochemical corrosion behaviour of dual-phase steels in 3.5% NaCl solution. *Materials Letters* Volume 59, Issues 19‑20, Pages 2488‑2491. (2005)

[56] A. JOSHI and D. F. STEIN. Chemistry of Grain Boundaries and Its Relation to Intergranular Corrosion of Austenitic Stainless Steel. *Corrosion* volume 28, issue 9. (1972)

[57] Ayodele C.O, Nenuwa O.B. Investigation of the Effects of Heat Treatment on the Corrosion Behaviour of Welded Low Carbon Steel in Different Environments. *International Journal of Science and Technology*. Volume 3 No. 8. (2013)

[58] Masumoto, T. and K. Hashimoto. Chemical properties of amorphous metals. *Ann. Rev. Mater. Sci*. 8: 215–233. (1978)

[59] T. Masumoto and K. Hashimoto. Corrosion properties of amorphous metals. *Physics* 41, C8-894 (1980)

[60] M.L. Morrison et al., “The Electrochemical Evaluation of a Zr-based Bulk Metallic Glass in a Phosphatebuffered Saline Electrolyte,” *J. Biomedical Materials Research Part A*, 74A (3), pp. 430–438. (2005)

[61] Zhu, S.L., X.M. Wang, F.X. Qin, and A. Inoue. A new Ti-based bulk glassy alloy with potential for biomedical application. *Mater. Sci. Eng. A* 459: 233–237. (2007)

[62] R.B. Diegle, N.R. Sorensen, T. Tsuru, R.M. Latanision, in: J.C. Scully (Ed.), *Treatise on Materials Science and Technology*, vol. 23, Academic Press, New York. (1983)

[63] Asami, K., K. Hashimoto, T. Masumoto, and S. Shimodaira. XPS study of the passive film on an extremely corrosion-resistant amorphous iron alloy. *Corrosion Sci*. 16: 909–914. (1976).

[64] Naka, M., K. Hashimoto, and T. Masumoto. High corrosion resistance of Cr-bearing amorphous Fe alloys in neutral and acidic solutions containing chloride. *Corrosion* 32: 146–152. (1976)

[65] Pang, S.J., T. Zhang, K. Asami, and A. Inoue. Formation of bulk glassy Fe75-x-yCrxMoyC15B10 alloys and their corrosion behavior. *J. Mater. Res*. 17: 701–704. (2002)

[66] K. Hashimoto. In pursuit of new corrosion-resistant alloys. *Corrosion Sci*. Vol. 58, No. 9. 715-722. (2002)

[67] Z. L. Long, C. T. Chang, Y. H. Ding, Y. Shao, P. Zhang, B. L. Shen and A. Inoue: ‘Corrosion behavior of Fe-based ferromagnetic (Fe, Ni)–B–Si–Nb

bulk glassy alloys in aqueous electrolytes', *J. Non-Cryst. Solids*, 354, 4609–4613. (2008)

[68] Shen, B.L., M. Akiba, and A. Inoue. Effect of Cr addition on the glass-forming ability, magnetic properties, and corrosion resistance of FeMoGaPCBSi bulk glassy alloys. *J. Appl. Phys*. 100: 043523-1–043523-5. (2006)

[69] Pang, S.J., T. Zhang, K. Asami, and A. Inoue. Synthesis of Fe–Cr– Mo–C–B–P bulk metallic glasses with high corrosion resistance. *Acta Mater*. 50: 489–497. (2002)

[70] Asami, K., S.J. Pang, T. Zhang, and A. Inoue. Preparation and corrosion resistance of Fe–Cr–Mo–C–B–P bulk glassy alloys. *J. Electrochem. Soc*. 149: B366–B369. (2002)

[71] Matusita, K. & Sakka, S. Kinetic study on non-isothermal crystallization of glass by thermal analysis. *Bulletin of the Institute for Chemical Research*, 59, 3, pp. 159-171, 1747-5198. (1981)

[72] M. Madinehei, P. Bruna, M. J. Duarte, E. Pineda, J. Klemm, and F. U. Renner. "Glass-formation and corrosion properties of Fe–Cr–Mo–C–B glassy ribbons with low Cr content." *Journal of Alloys and Compounds* 615: S128-S131. (2014)

[73] Chen, H.S. Structural relaxation in metallic glasses. In Amorphous Metallic Alloys, ed. F.E. Luborsky, pp. 169–186. *London, U.K.: Butterworths*. (1983)

[74] J. J. Lewandowski, W. H. Wang and A. L. Greer. Intrinsic plasticity or brittleness of metallic glasses. *Philosophical Magazine letters*, Vol. 85, No. 2, 77-87. (2005)

[75] Long, Z.L., B.L. Shen, Y. Shao, C.T. Chang, Y.Q. Zeng, and A. Inoue. Corrosion behaviour of [(Fe0.6Co0.4)0.75B0.2Si0.05]96Nb4 bulk glassy alloy in sulphuric acid solutions. *Mater. Trans*. 47: 2566–2570. (2006)

[76] S. Sheng, C. Ma, S. Pang and T. Zhang. Glass-Forming Ability and Mechanical Properties of Sm-Doped Fe–Cr–Mo–C–B Glassy Alloys. *Materials Transactions*, Vol. 46, No. 12 pp. 2949 to 2953. (2005)

[77] M.J. Duarte, A. Kostka, J.A. Jimenez, P. Choi, J. Klemm, D. Crespo, et al., Crystallization, phase evolution and corrosion of Fe-based metallic glasses: An atomic-scale structural and chemical characterization study, *Acta Mater*. 71 20–30. (2014)

[78] M.J. Duarte, J. Klemm, S.O. Klemm, K.J.J. Mayrhofer, M. Stratmann, S. Borodin, A. H. Romero, M. Madinehei, D. Crespo, J. Serrano, S. S. A. Gerstl, P. P. Choi, D. Raabe, F. U. Renner. Element-resolved corrosion analysis of stainless-type glass-forming steels., *Science.* 341 372–6. (2013)

[79] R. A. Freeman, D. C. Silverman, "Error Propagation in Coupon Immersion Tests", *Corrosion*, Vol.48, No.6, pp.463, (1988)

[80] R. Kirchheim, B. Heine, H. Fischmeister, S. Hofmann, H. Knote, U. Stolz, *Corros. Sci*. 29 899–917. (1989)

[81] J. Jayaraj, J.M. Park, P.F. Gostin, E. Fleury, A. Gebert, L. Schultz, *Intermetallics* 17 1120. (2009)

[82] S.L. Wang, S. Yi, *Intermetallics* 18 1950–1953. (2010)

[83] Y. Wang, S.L. Zheng, W. Ke, W. H. Sun, J.Q. Wang. Electrochemical behavior of Fe-based metallic glasses in acidic and neutral solutions. *Corrosion Science* 63 159-173. (2012)

[84] S. T. Arab, K. M. Emran, *Int. J. Appl. Chem*. 3(1), 69. (2007)

[85] Z. Zhou, L. Wang, F.C. Wang, H.F. Zhang, Y.B. Liu, S.H. Xu, *Surface and Coatings Technology* 204 563–570. (2009)

[86] K. Hashimoto. What we have learned from studies on chemical properties of amorphous alloys? *Applied Surface Science* 257 8141-8150. (2011)

[87] D. Rai, L. E. Eary and J. M. Zaghara. Environmental chemistry of chromium. *The Science of the total Environment*, 86 15-23. (1989)

[88] Salem, Farida Y., et al. "Kinetics of chromium transformations in the environment." *Science of the Total Environment* 86.1: 25-41. (1989)

[89] Haupt, S. and H-H. Strehblow. "A combined surface analytical and electrochemical study of the formation of passive layers on FeCr alloys in 0.5 MH 2 SO 4." *Corrosion Science* 37.1: 43-54. (1995)

[90] Robert Berger, Ulf Bexell, T. Mikael Grehk, Sven-Erik Hörnström. A comparative study of the corrosion protective properties of chromium and

chromium free passivation methods. *Surface & Coatings Technology* 202 391–397. (2007)

[91] J.P. Popic, D.M. Drazic. Electrochemistry of active chromium Part II. Three hydrogen evolution reactions on chromium in sulfuric acid. *Electrochimica Acta* 49 4877–4891. (2004)

[92] Beverskog, B., and I. Puigdomenech. "Revised Pourbaix diagrams for chromium at 25–300 C." *Corrosion Science* 39.1: 43-57. (1997)

[93] K. Hashimoto, K. Asami, A. Kawashima, H. Habazaki, E. Akiyama. The role of corrosion-resistant alloying elements in passivity. *Corrosion Science* 49 42-52. (2007)

[94] S. L. Wang, H. X. Li, X. F. Zhang, S. Yi. Effect of Cr contents in Fe-based bulk metallic glasses on the Glass forming ability and the corrosion resistance. *Materials Chemistry and Physics* 113 878-883. (2009)

[95] K. Asami, M. Naka, K. Hashimoto, and T. Masumoto. Effect of Molybdenum on the Anodic Behavior of Amorphous Fe-Cr-Mo-B Alloys in Hydrochloric Acid. *J. Electrochem. Soc*. 127(10): 2130-2138. (1980)

[96] M. Belkhaouda, L. Bazzi, A. Benlhachemi, R. Salghi, B. Hammouti, S. Kertit, Effect of the heat treatment on the corrosion behaviour of amorphous Fe–Cr–P–C–Si alloy in 0.5M H2SO4, *Appl. Surf. Sci*. 252 7921–7925. (2006)

[97] C.A.C. Souza, F.S. Politi, C.S. Kiminami, Influence of structural relaxation and partial devitrification on the corrosion resistance of Fe78B13Si9 amorphous alloy, *Scr. Mater.* 39 329–334. (1998)

[98] R. Raicheff, V. Zaprianova, E. Gattef, Effect of structural relaxation on electrochemical corrosion behaviour of amorphous alloys, *J. Mater. Sci. Lett*. 16 1701–1704. (1997)

[99] H. Habazaki, A. Kawashima, K. Asami, K. Hashimoto, The effect of structural relaxation on the passivation behavior of amorphous Fe-Cr-W-P-C alloys, *Corros. Sci*. 31 343–348. (1990)

[100] C.A.C. Souza, S.E. Kuri, F.S. Politti, J.E. May, C.S. Kiminami, Corrosion resistance of amorphous and polycrystalline FeCuNbSiB alloys in sulphuric acid solution, *J. Non. Cryst. Solids*. 247 69–73. (1999)

[101] C.S. Kiminami, C.A.C. Souza, L.F. Bonavina, L.R.P. de Andrade Lima, S. Suriñach, M.D. Baró, et al., Partial crystallization and corrosion resistance of amorphous Fe-Cr-M-B (M=Mo, Nb) alloys, *J. Non. Cryst. Solids*. 356 2651–2657. (2010)

[102] Y. Yang, C. Zhang, Y. Peng, Y. Yu, L. Liu, Effects of crystallization on the corrosion resistance of Fe-based amorphous coatings, *Corros. Sci*. 59 10–19. (2012)

[103] C.A.. Souza, J.. May, L. Bolfarini, S.. Kuri, M.. de Oliveira, C.. Kiminami, Influence of composition and partial crystallization on corrosion resistance of amorphous Fe–M–B–Cu (M=Zr, Nb, Mo) alloys, *J. Non. Cryst. Solids*. 284 99–104. (2001)

[104] M.S. Bakare, K.T. Voisey, K. Chokethawai, D.G. McCartney, Corrosion behaviour of crystalline and amorphous forms of the glass forming alloy Fe43Cr16Mo16C15B10, *J. Alloys Compd*. 527 210–218. (2012)

[105] A. Pardo, M.C. Merino, E. Otero, M.D. López, A. M'hich, Influence of Cr additions on corrosion resistance of Fe- and Co-based metallic glasses and nanocrystals in H2SO4, *J. Non. Cryst. Solids*. 352 3179–3190. (2006)

[106] M. Bojinov, I. Betova, R. Raicheff, Influence of molybdenum on the transpassivity of a Fe + 12%Cr alloy in H2SO4 solutions, *J. Electroanal. Chem*. 430 169–178. (1997)

[107] Schuh, C.A., T.C. Hufnagel, and U. Ramamurty. Mechanical behavior of amorphous alloys. *Acta Mater*. 55: 4067–4109. (2007)

[108] Dmitri V. Louzguine-Luzgin, Larissa V. Louzguina-Luzgina and Alexander Yu. Churyumov. Mechanical Properties and Deformation Behavior of Bulk Metallic Glasses. *Metals*, 3, 1-22. (2013)

[109] X.J. Gu, S.J. Poon, G.J. Shiflet, *J. Mater. Res*. 22 344–351. (2007)

[110] Guo Sheng-feng, Wang Jing-feng, Zhang Hong-ju, Xie Sheng-hui. Enhanced plasticity of Fe-based bulk metallic glass by tailoring microstructure. *Trans. Nonferrous Met. Soc. China* 22 348−353. (2012)

[111] Makino, A., Li, X., Yubuta, K., Chang, C., Kubota, T., & Inoue, A. The effect of Cu on the plasticity of Fe–Si–B–P-based bulk metallic glass. *Scripta Materialia*, *60*(5), 277-280. (2009)

[112] X. J. Gu, A. G. McDermott, S. J. Poon and G. J. Shiflet: 'Critical Poisson's ratio for plasticity in Fe–Mo–C–B–Ln bulk amorphous steel', *Appl. Phys. Lett*., 88, 211905-1–211905-3. (2006)

[113] Lewandowski JJ, Wang WH, Greer AL. *Philos Mag Lett* ;85:77. (2005)

[114] A. L. Greer, Y. Q. Cheng, E. Ma. Shear bands in metallic glasses. *Materials Science and Engineering* R 74 71–132. (2013)

[115] C.E. Packard, C.A. Schuh. Initiation of shear bands near a stress concentration in metallic glass. *Acta Materialia* 55 5348–5358. (2007)

[116] W. C. Oliver, G. M. Pharr. An improved technique for determining hardness and elastic modulus using load and displacement sensing indentation. *J. Mater. Res*., Vol. 7, No. 6. (1992)

[117] D. J. Brangan, Yali. Tang. Developing extreme hardness (>15GPa) in iron based nanocomposites. *Composites*: Part A 33 855-859. (2002)

[118] A. Leyland, A. Matthews. On the significance of the H/E ratio in wear control: a nanocomposite coating approach to optimized tribological behavior. *Wear* 246 1-11. (2000)

[119] T. L. Oberle. Properties influencing wear of metals. *J. Appl. Phys*. 24 981. (1953)